IOP Publishing

Nanoscale Energy Transport
Emerging phenomena, methods and applications
Bolin Liao

Chapter 2

Higher-order phonon scattering: advancing the quantum theory of phonon linewidth, thermal conductivity and thermal radiative properties

Tianli Feng and Xiulin Ruan

Phonon scattering plays a central role in the quantum theory of phonon linewidth, which in turn governs important properties including infrared spectra, Raman spectra, lattice thermal conductivity, thermal radiative properties, and also significantly affects other important processes such as hot electron relaxation. Since Maradudin and Fein's classic work in 1962, three-phonon scattering had been considered as the dominant intrinsic phonon scattering mechanism and has seen tremendous advances. However, the role of the higher-order four-phonon scattering had been persistently unclear and so was ignored. The tremendous complexity of the formalism and computational challenges stood in the way, prohibiting the direct and quantitative treatment of four-phonon scattering. In 2016, a rigorous four-phonon scattering formalism was developed, and the prediction was realized using empirical potentials. In 2017, the method was extended using first-principles calculated force constants, and the thermal conductivities of boron arsenides (BAs), Si and diamond were predicted. The predictions for BAs were later confirmed by several independent experiments. Four-phonon scattering has since been investigated in a range of materials and established as an important intrinsic scattering mechanism for thermal transport and radiative properties. Specifically, four-phonon scattering is important when the fourth-order scattering potential or phase space becomes relatively large. The former scenario includes: (i) nearly all materials when the temperature is high; (ii) strongly anharmonic (low thermal conductivity) materials, including most rocksalt compounds, halides, hydrides, chalcogenides and oxides. The latter scenario includes: (iii) materials with large acoustic–optical phonon band gaps, such as XY compounds with a large atomic mass ratio between X and Y; (iv) two-dimensional materials with reflection symmetry, such as single-layer graphene, single-layer boron nitride and carbon nanotubes; and (v) phonons with a large

doi:10.1088/978-0-7503-1738-2ch2

density of states, such as optical phonons, which are important for Raman, infrared and thermal radiative properties. Four-phonon scattering is expected to gain broad interest in various technologically important materials for thermoelectrics, thermal barrier coatings, thermal energy storage, phase change, nuclear power, ultra-high temperature ceramics, infrared spectra, Raman spectra, radiative transport, hot electron relaxation and radiative cooling. Four-phonon scattering has been, and will continue to be, established as an important intrinsic phonon scattering mechanism beyond three-phonon scattering. The prediction of four-phonon scattering will transition from a breakthrough to a new routine in the next decade.

2.1 Overview

Phonon scattering plays a central role in the quantum theory of phonon linewidth, thermal conductivity and thermal radiative properties. For over half a century, three-phonon scattering has been considered as the dominant intrinsic phonon scattering mechanism. Starting from the third-order anharmonic Hamiltonian and Fermi's golden rule (FGR), Maradudin and Flinn [1], Maradudin and Fein [2], and Maradudin *et al* [3] derived an anharmonic lattice dynamics (ALD) method to predict intrinsic three-phonon scattering rates in solids. Debernardi *et al* [4] combined ALD and first-principles methods based on the density functional theory (DFT) to predict three-phonon scattering rates and linewidths for carbon, silicon and germanium, and the results agreed well with Raman spectra. This work was followed by the first-principles prediction of the phonon linewidths of a variety of materials [5–8]. More recently, Broido *et al* combined first-principles calculations of three-phonon scattering rates and the phonon Boltzmann transport equation (BTE) and enabled first-principles prediction of thermal conductivity [9]. Many studies have since been conducted on the thermal transport based on three-phonon scattering, and the calculated thermal conductivity (κ) has found incredible agreement with measured κ values for a variety of systems [9–15]. First-principles calculations of three-phonon scattering rates of zone-center optical phonons have also been combined with the Lorentz oscillator model to predict the thermal radiative properties of polar materials [16].

However, a persistent fundamental question remained: what is the role of four-phonon and higher-order scattering? The observations of a series of experiments deviated from the three-phonon scattering theory, but no accepted explanation had emerged. In the early years, Joshi *et al* found in experiments that the thermal conductivity of silicon at a high temperature decreases more rapidly than the $1/T$ trend as would be given by the three-phonon scattering theory, and they assumed the existence of four-phonon scattering to be responsible for this behavior [17]. However, Ecsedy and Klemens made calculations and concluded that this trend could not be due to four-phonon scattering [18]. The optical phonon linewidths based on three-phonon theory often show large underestimation for materials with significant infrared applications such as cubic BN (*c*-BN), 3*C*-SiC, GaN, GaP, GaAs, InAs and AlAs at high temperature or even room temperature (RT) [4, 19, 20]. Moreover, first-principles methods overestimated the measured thermal conductivities of a

number of materials [10, 11, 21–23]. For example, while some predictions gave reasonable accuracy with measured data at low temperature, they over-predicted significantly at higher temperature [10], diminishing the predictive power for applications such as thermal barrier coatings and high temperature thermoelectrics. Even at RT, such deviations could become quite large for some technologically important materials [11, 21–23]. Such deviations had often been attributed to defects and impurities in the materials, and the role of four-phonon scattering was unclear and ignored, largely due to the lack of theoretical formalism and computational power needed to treat four-phonon scattering. Recent explorations of four-phonon scattering included checking the phase space [24] and examining its significance from molecular dynamics [25]. Direct and quantitative prediction of four-phonon scattering rates was greatly desired to uncover the physics but was not available.

In 2016, Feng and Ruan [26] developed the four-phonon scattering formalism and mitigated the challenges in computation, and rigorously predicted the four-phonon scattering rates for several benchmark materials such as diamond, silicon, germanium and solid argon. Based on empirical interatomic potentials, they predicted strong four-phonon scattering rates in silicon and germanium at high temperatures and in argon even at low temperatures. Their four-phonon scattering results have explained well the discrepancy in phonon scattering rates between the perturbation theory of three-phonon scattering and molecular dynamics (MD) using the same empirical potentials, because MD naturally includes all the orders of anharmonicity. The inclusion of four-phonon scattering makes the ALD and MD consistent with each other, and pushes a step forward towards the 'unification' of these simulation methods of phonon and thermal transport.

In 2017, Feng *et al* [27] extended the method by calculating the fourth-order force constants from DFT instead of empirical interatomic potentials and predicted a significant impact of four-phonon scattering on the thermal conductivity of diamond and silicon at high temperatures and BAs even at RT. Their predictions for Si agree well with early experiments, and those for BAs were later verified by three independent experimental works published in 2018 that directly measured the thermal conductivity of high-quality single-crystal BAs [28–30]. Since then, the prediction of the large impact of four-phonon scattering has been accepted, and more investigations are going on. For example, its significance was recently found in two-dimensional material graphene [31] and other strongly anharmonic materials such as PbTe [32] and NaCl [33].

Compared to three-phonon scattering, the most apparent complexity of four-phonon scattering is its large phase space. As illustrated in figure 2.1, in a three-phonon process, a phonon mode λ can either split into two other modes ($\lambda \rightarrow \lambda_1 + \lambda_2$) or combine with one other mode to a new one ($\lambda + \lambda_1 \rightarrow \lambda_2$). In a four-phonon process, it can split into three other modes ($\lambda \rightarrow \lambda_1 + \lambda_2 + \lambda_3$), generate two new modes by absorbing one ($\lambda + \lambda_1 \rightarrow \lambda_2 + \lambda_3$), or convert to a new mode by absorbing two ($\lambda + \lambda_1 + \lambda_2 \rightarrow \lambda_3$). All these processes must obey the conservation law of energy and quasi-momentum. The number of possible combinations of four-phonon modes that satisfy the conservation laws is usually several orders larger than

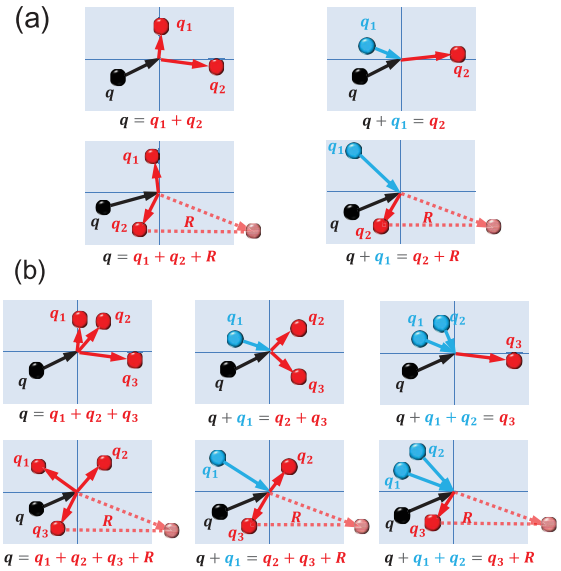

Figure 2.1. Three- and four-phonon scattering diagrams. (a) Three-phonon splitting and combination processes. (b) Four-phonon splitting, redistribution and combination processes. The shaded rectangles represent the first Brillouin zone (BZ). The phonon momentum is $\hbar\mathbf{q}$. The processes with momentum conserved are normal processes. The others with momentum non-conserved are Umklapp processes, in which the resulting phonons are folded back by reciprocal lattice vectors $\mathbf{R}$. Reproduced with permission from [27]. Copyright 2017 the American Physical Society.

that of three-phonon processes. For example, in silicon, by using a $16 \times 16 \times 16$ **q**-mesh, a phonon mode can find $\sim 10^3$ possible combinations with other modes for three-phonon processes, while it can find 10^7–10^8 possible combinations for four-phonon scattering. Therefore, four-phonon scattering is less dependent on the dispersive nature of phonon frequencies compared to three-phonon scattering.

Feng *et al*'s works [26, 27, 31] have established that four-phonon scattering is non-negligible with two origins: strong scattering potential and large scattering phase space. The former presents as strong anharmonicity, as found in strongly anharmonic materials, i.e. most low thermal conductivity materials such as solid argon [26], PbTe [32] and NaCl [33]. Even for weakly anharmonic materials with high thermal conductivity, such as diamond and silicon, the anharmonicity could become strong when the temperature is high. For example, four-phonon scattering reduces the thermal conductivity of silicon by 30% at 1000 K [26, 27]. Quantitatively, four-phonon scattering rates scale with temperature quadratically ($\sim T^2$), which is one order faster than three-phonon scattering. Regarding the scattering phase space, the four-phonon process generally has a several orders larger phase space than three-phonon scattering since the conservation laws can easily be satisfied. This effect is reflected most significantly in higher-frequency phonons including, in particular, optical phonons, which have a large density of states and thus four-phonon scattering phase space. In addition, the four-phonon scattering can be exceptionally important in systems where three-phonon processes

have a suppressed phase space, either due to a large acoustic–optical phonon band gap or the reflection symmetry in 2D materials. One example of the former is BAs, a quite harmonic crystal, for which neglecting four-phonon scattering leads to 57% over-prediction in thermal conductivity at room temperature [27]. The optical phonon relaxation times in these materials with large acoustic–optic phonon band gaps are exceptionally suppressed by four-phonon scattering [27]. Single-layer graphene is an example of the latter, and the four-phonon scattering for the flexural acoustic (ZA) mode was predicted to be suppressed less than the three-phonon scattering by reflection symmetry [31], although the prediction still needs experimental validation.

Beyond the single-mode relaxation time approximation (SMRTA or RTA), Feng and Ruan [31] derived the exact solution to phonon BTE that incorporates the four-phonon scattering's phase space into the iteration in the calculation of thermal conductivity. Due to the large phase space of four-phonon scattering, the iteration is extremely computationally expensive. Fortunately, they found that four-phonon scattering is usually dominated by the Umklapp process even in the materials where three-phonon scattering is dominated by the normal process [26, 27], indicating that in order to save time it is not necessary to include the four-phonon's phase space in the iterative scheme in these materials. However, for some materials such as graphene where the four-phonon scattering is dominated by the normal process, the iterative scheme involving four-phonon phase space is crucial to the thermal conductivity prediction [31].

The remainder of this chapter is organized as follows. In section 2.2, the four-phonon scattering formalism is derived in the context of solving phonon BTE. For generality, multiple scattering mechanisms including three-phonon, four-phonon, phonon–impurity and phonon–boundary scatterings are included in the solution since they are coupled together with each other in the exact solution that involves the iteration of the phase spaces of these scattering processes. The SMRTA solution is presented at the zeroth iteration. In section 2.3, the significance of four-phonon scattering induced by large scattering potential is presented. For weakly anharmonic materials, the large four-phonon scattering potential could be induced by raising the temperature. For strongly anharmonic materials, the strong four-phonon scattering potential is caused by the intrinsic strongly anharmonic interatomic bonding, even at low temperatures. In section 2.4, the significance of four-phonon scattering induced by large scattering phase space is presented. This is either induced by restricted three-phonon scattering phase space or a large density of states (DOS). The former includes certain groups of materials such as those with large acoustic–optical phonon band gaps and two-dimensional materials with reflection symmetry. The latter is remarkably represented in optical phonon modes, which often show high four-phonon scattering rates due to large DOS. The prediction of zone-center optical phonon linewidth and thermal radiative properties is extensively presented here. In section 2.5, we supplement some discussion of a few important issues related to four-phonon scattering such as the frequency scaling law, the Umklapp scattering and the three-phonon scattering to the second order. In section 2.6, a brief summary is provided and an outlook of future research directions is presented.

2.2 Formalism of four-phonon scattering

In this section, we derive the solution to the phonon BTE that includes three-phonon, four-phonon, phonon–impurity and phonon–boundary scattering. The derivation is extensively presented in [26, 31], and it is summarized here again. The phonon BTE [34–36]

$$\mathbf{v}_\lambda \cdot \nabla n_\lambda = \left.\frac{\partial n_\lambda}{\partial t}\right|_s \tag{2.1}$$

describes the balance of the phonon population between diffusive drift and collision. λ labels the phonon mode ($\mathbf{q}$, ν), with $\mathbf{q}$ representing the wave vector and ν representing the dispersion branch, $\mathbf{v}_\lambda$ is the group velocity, and n_λ is the phonon occupation number. Due to a small temperature gradient, n_λ has a small derivation n'_λ from its equilibrium Bose–Einstein distribution $n^0_\lambda = [\exp(\hbar\omega_\lambda/k_\mathrm{B}T) - 1]^{-1}$ so that $n_\lambda = n^0_\lambda + n'_\lambda$. By assuming that n'_λ is independent of temperature [35], $(\partial n_\lambda/\partial T) \simeq (\partial n^0_\lambda/\partial T)$, we have

$$\mathbf{v}_\lambda \cdot \nabla T \frac{\partial n^0_\lambda}{\partial T} = \left.\frac{\partial n'_\lambda}{\partial t}\right|_s \tag{2.2}$$

considering $\nabla n_\lambda = (\partial n_\lambda/\partial T)\nabla T$.

The scattering term $(\partial n'_\lambda/\partial t)|_s$ is the decay rate of the perturbation n'_λ due to the scattering processes of the mode λ, including the three-phonon processes $\lambda \rightarrow \lambda_1 + \lambda_2$ and $\lambda + \lambda_1 \rightarrow \lambda_2$, the four-phonon processes $\lambda \rightarrow \lambda_1 + \lambda_2 + \lambda_3$, $\lambda + \lambda_1 \rightarrow \lambda_2 + \lambda_3$ and $\lambda + \lambda_1 + \lambda_2 \rightarrow \lambda_3$, and the isotope and boundary scattering processes $\lambda \rightarrow \lambda_1$. The scattering rates of these processes are given by the scattering probabilities, P, which are determined by FGR:

$$P_{i\rightarrow f} = \frac{2\pi}{\hbar} |\langle f|\hat{H}|i\rangle|^2 \, \delta(E_i - E_f), \tag{2.3}$$

where $|i\rangle$ and $|f\rangle$ are the initial and final quantum states, respectively. The net transition rate from $|i\rangle$ to $|f\rangle$ is, therefore, written as

$$P_{i\rightarrow f} - P_{f\rightarrow i} = \frac{2\pi}{\hbar}\left(|\langle f|\hat{H}|i\rangle|^2 - |\langle i|\hat{H}|f\rangle|^2\right)\delta(E_i - E_f). \tag{2.4}$$

The initial and final quantum states depend on scattering processes. For example, for the three-phonon process $\lambda \rightarrow \lambda_1 + \lambda_2$, the initial and final quantum states are $|i\rangle = |n_\lambda + 1, n_{\lambda_1}, n_{\lambda_2}\rangle$ and $|f\rangle = |n_\lambda, n_{\lambda_1} + 1, n_{\lambda_2} + 1\rangle$, respectively. Similarly, for the four-phonon process $\lambda \rightarrow \lambda_1 + \lambda_2 + \lambda_3$, the initial and final quantum states are $|i\rangle = |n_\lambda + 1, n_{\lambda_1}, n_{\lambda_2}, n_{\lambda_3}\rangle$ and $|f\rangle = |n_\lambda, n_{\lambda_1} + 1, n_{\lambda_2} + 1, n_{\lambda_3} + 1\rangle$, respectively. The other processes can be analogized.

The transition rate in equation (2.4) is determined by the lattice Hamiltonian $\hat{H}$ [2, 37]:

$$\hat{H} = \hat{H}_0 + \hat{H}_3 + \hat{H}_4 + \cdots + \hat{H}_\mathrm{iso} + \cdots, \tag{2.5}$$

which includes the harmonic part

$$\hat{H}_0 = \sum_{\lambda} \hbar\omega_{\lambda}\left(a_{\lambda}^{\dagger}a_{\lambda} + 1/2\right), \tag{2.6}$$

the first-order anharmonic part

$$\hat{H}_3 = \sum_{\lambda\lambda_1\lambda_2} H^{(3)}_{\lambda\lambda_1\lambda_2}\left(a^{\dagger}_{-\lambda} + a_{\lambda}\right)\left(a^{\dagger}_{-\lambda_1} + a_{\lambda_1}\right)\left(a^{\dagger}_{-\lambda_2} + a_{\lambda_2}\right), \tag{2.7}$$

with

$$H^{(3)}_{\lambda\lambda_1\lambda_2} = \frac{\hbar^{3/2}}{2^{3/2}\times 6N_{\mathbf{q}}^{1/2}}\Delta_{\mathbf{q}+\mathbf{q}_1+\mathbf{q}_2,\mathbf{R}}\frac{V^{(3)}_{\lambda\lambda_1\lambda_2}}{\sqrt{\omega_{\lambda}\omega_{\lambda_1}\omega_{\lambda_2}}}, \tag{2.8}$$

$$V^{(3)}_{\lambda\lambda_1\lambda_2} = \sum_{b,l_1b_1,l_2b_2}\sum_{\alpha\alpha_1\alpha_2}\Phi^{\alpha\alpha_1\alpha_2}_{0b,l_1b_1,l_2b_2}\frac{\mathrm{e}^{\lambda}_{\alpha b}\mathrm{e}^{\lambda_1}_{\alpha_1 b_1}\mathrm{e}^{\lambda_2}_{\alpha_2 b_2}}{\sqrt{\bar{m}_b\bar{m}_{b_1}\bar{m}_{b_2}}}\mathrm{e}^{\mathrm{i}\mathbf{q}_1\cdot\mathbf{r}_{l_1}+\mathrm{i}\mathbf{q}_2\cdot\mathbf{r}_{l_2}}, \tag{2.9}$$

the second-order anharmonic part

$$\hat{H}_4 = \sum_{\lambda\lambda_1\lambda_2\lambda_3} H^{(4)}_{\lambda\lambda_1\lambda_2\lambda_3}\left(a^{\dagger}_{-\lambda} + a_{\lambda}\right)\left(a^{\dagger}_{-\lambda_1} + a_{\lambda_1}\right)\left(a^{\dagger}_{-\lambda_2} + a_{\lambda_2}\right)\left(a^{\dagger}_{-\lambda_3} + a_{\lambda_3}\right) \tag{2.10}$$

with

$$H^{(4)}_{\lambda\lambda_1\lambda_2\lambda_3} = \frac{\hbar^2}{2^2\times 24N_{\mathbf{q}}}\Delta_{\mathbf{q}+\mathbf{q}_1+\mathbf{q}_2+\mathbf{q}_3,\mathbf{R}}\frac{V^{(4)}_{\lambda\lambda_1\lambda_2\lambda_3}}{\sqrt{\omega_{\lambda}\omega_{\lambda_1}\omega_{\lambda_2}\omega_{\lambda_3}}} \tag{2.11}$$

$$\begin{aligned} V^{(4)}_{\lambda\lambda_1\lambda_2\lambda_3} = &\sum_{b,l_1b_1,l_2b_2,l_3b_3}\sum_{\alpha\alpha_1\alpha_2\alpha_3}\Phi^{\alpha\alpha_1\alpha_2\alpha_3}_{0b,l_1b_1,l_2b_2,l_3b_3} \\ &\times\frac{\mathrm{e}^{\lambda}_{\alpha b}\mathrm{e}^{\lambda_1}_{\alpha_1 b_1}\mathrm{e}^{\lambda_2}_{\alpha_2 b_2}\mathrm{e}^{\lambda_3}_{\alpha_3 b_3}}{\sqrt{\bar{m}_b\bar{m}_{b_1}\bar{m}_{b_2}\bar{m}_{b_3}}}\mathrm{e}^{\mathrm{i}\mathbf{q}_1\cdot\mathbf{r}_{l_1}+\mathrm{i}\mathbf{q}_2\cdot\mathbf{r}_{l_2}+\mathrm{i}\mathbf{q}_3\cdot\mathbf{r}_{l_3}}, \end{aligned} \tag{2.12}$$

and the extrinsic perturbations such as the isotopes

$$\hat{H}_{\mathrm{iso}} = \sum_{\lambda\lambda_1} H^{(\mathrm{iso})}_{\lambda\lambda_1}\left(a^{\dagger}_{-\lambda} + a_{\lambda}\right)\left(a^{\dagger}_{-\lambda_1} + a_{\lambda_1}\right) \tag{2.13}$$

with

$$H^{(\mathrm{iso})}_{\lambda\lambda_1} = -\frac{1}{4N_{\mathbf{q}}}\sum_{l,b}\sum_{\mathbf{q}_l}\Delta m_{l,\,b}\sqrt{\omega_{\lambda}\omega_{\lambda_1}}\Delta_{\mathbf{q}+\mathbf{q}_1+\mathbf{q}_l,\,\mathbf{R}}\mathbf{e}^{\lambda}_{b}\cdot\mathbf{e}^{\lambda_1}_{b}\mathrm{e}^{-\mathrm{i}\mathbf{q}_l\cdot\mathbf{r}_l}, \tag{2.14}$$

where b, l and α label the indices of the basis atom, unit cell and direction, respectively. $N_{\mathbf{q}}$ is the total number of $\mathbf{q}$ points of a uniform mesh in the first BZ. The Kronecker delta $\Delta_{i,j}$ is 0 if $i \neq j$ or 1 if $i = j$. $\mathbf{e}$ is the phonon eigenvector. The summation of $\sum_{l,b}$ goes over all the unit cells in the domain and the summation over

$\mathbf{q}_{1,2,3,I}$ goes over all the $\mathbf{q}$ points in the first BZ. $a^{\dagger}$ and a are the phonon creation and annihilation operators, respectively. $\mathbf{R}$ represents any reciprocal lattice vector that can be decomposed into the superposition of integer reciprocal lattice basis vectors. Φ is the interatomic force constant (IFCs). $\mathbf{r}_l$ is the position vector of the lth unit cell. (Attention should be paid to the usage of $\mathbf{e}$ and $\mathbf{r}_l$ as discussed at the end of this section.)

Substituting equation (2.5) into equation (2.4), the right-hand side of (2.2) can be rewritten as [2, 13, 26, 34–40]

$$\begin{aligned}\left.\frac{\partial n'_\lambda}{\partial t}\right|_s = & -\sum_{\lambda_1\lambda_2}\left\{\frac{1}{2}[n_\lambda(1+n_{\lambda_1})(1+n_{\lambda_2})-(1+n_\lambda)n_{\lambda_1}n_{\lambda_2}]\mathcal{L}_- \right.\\ & \left.+[n_\lambda n_{\lambda_1}(1+n_{\lambda_2})-(1+n_\lambda)(1+n_{\lambda_1})n_{\lambda_2}]\mathcal{L}_+\right\}\\ & -\sum_{\lambda_1\lambda_2\lambda_3}\left\{\frac{1}{6}[n_\lambda(1+n_{\lambda_1})(1+n_{\lambda_2})(1+n_{\lambda_3})-(1+n_\lambda)n_{\lambda_1}n_{\lambda_2}n_{\lambda_3}]\mathcal{L}_{--}\right.\\ & +\frac{1}{2}[n_\lambda n_{\lambda_1}(1+n_{\lambda_2})(1+n_{\lambda_3})-(1+n_\lambda)(1+n_{\lambda_1})n_{\lambda_2}n_{\lambda_3}]\mathcal{L}_{+-}\\ & \left.+\frac{1}{2}[n_\lambda n_{\lambda_1}n_{\lambda_2}(1+n_{\lambda_3})-(1+n_\lambda)(1+n_{\lambda_1})(1+n_{\lambda_2})n_{\lambda_3}]\mathcal{L}_{++}\right\}\\ & -\sum_{\lambda_1}(n_\lambda-n_{\lambda_1})\mathcal{L}_{\mathrm{iso}}-(n_\lambda-n^0_\lambda)\frac{1}{\tau^0_{b,\lambda}}.\end{aligned} \tag{2.15}$$

The first summation on the right-hand side represents the three-phonon scattering rate of the mode λ, with the first term accounting for the splitting process $\lambda \rightarrow \lambda_1+\lambda_2$ and the second the combination process $\lambda+\lambda_1 \rightarrow \lambda_2$. The physical meaning of the first term is the difference between the transition rates of $\lambda \rightarrow \lambda_1+\lambda_2$ and $\lambda \leftarrow \lambda_1+\lambda_2$ and thus indicates the decay rate of n_λ due to the splitting process. Similarly, the second term illustrates the transition rate difference between $\lambda+\lambda_1 \rightarrow \lambda_2$ and $\lambda+\lambda_1 \leftarrow \lambda_2$, indicating the decay rate of n_λ due to the combination process. $\mathcal{L}_\pm$ contains the information of the intrinsic transition probability and the transition selection rules for energy and momentum, $\omega_\lambda \pm \omega_{\lambda_1}-\omega_{\lambda_2}=0$ and $\mathbf{q}\pm\mathbf{q}_1-\mathbf{q}_2=\mathbf{R}$, where $\mathbf{R}=0$ implies the normal (N) process and $\mathbf{R}\neq 0$ the Umklapp (U) process. The second summation accounts for the four-phonon scattering of mode λ, with the first parenthesis representing the process $\lambda \rightarrow \lambda_1+\lambda_2+\lambda_3$, the second the process $\lambda+\lambda_1 \rightarrow \lambda_2+\lambda_3$ and the third $\lambda+\lambda_1+\lambda_2 \rightarrow \lambda_3$. Similarly, $\mathcal{L}_{\pm\pm}$ accounts for the transition probabilities and the selection rules, i.e., $\omega_\lambda \pm \omega_{\lambda_1} \pm \omega_{\lambda_2}-\omega_{\lambda_3}=0$ and $\mathbf{q}\pm\mathbf{q}_1\pm\mathbf{q}_2-\mathbf{q}_3=\mathbf{R}$, for those processes. The third summation is the phonon–isotope scattering rate for $\lambda \rightarrow \lambda_1$ given by Tamura [37], with the selection rules $\omega_\lambda=\omega_{\lambda_1}$ and $\mathbf{q}\neq\mathbf{q}_1$. The last term on the right-hand side of equation (2.15) indicates the phonon–boundary scattering rate. The minus sign before each scattering term indicates that the perturbation n'_λ is decreasing with time, i.e. the phonon distribution tends to recover its equilibrium state due to the scattering. The expressions for $\mathcal{L}_\pm$, $\mathcal{L}_{\pm\pm}$ and $\mathcal{L}_{\mathrm{iso}}$ are given as

$$\mathcal{L}_{\pm} = \frac{\pi\hbar}{4N_{\mathbf{q}}} \left| V_{\pm}^{(3)} \right|^2 \Delta_{\pm} \frac{\delta(\omega_{\lambda} \pm \omega_{\lambda_1} - \omega_{\lambda_2})}{\omega_{\lambda}\omega_{\lambda_1}\omega_{\lambda_2}}, \tag{2.16}$$

$$\mathcal{L}_{\pm\pm} = \frac{\pi\hbar}{4N_{\mathbf{q}}} \frac{\hbar}{2N_{\mathbf{q}}} \left| V_{\pm\pm}^{(4)} \right|^2 \Delta_{\pm\pm} \frac{\delta(\omega_{\lambda} \pm \omega_{\lambda_1} \pm \omega_{\lambda_2} - \omega_{\lambda_3})}{\omega_{\lambda}\omega_{\lambda_1}\omega_{\lambda_2}\omega_{\lambda_3}}, \tag{2.17}$$

$$\mathcal{L}_{\text{iso}} = \frac{\pi}{2N_{\mathbf{q}}} \omega_{\lambda}\omega_{\lambda_1} \sum_{b}^{n} g_b \left| \mathbf{e}_{\lambda}^{b} \cdot \mathbf{e}_{\lambda_1}^{b*} \right|^2 \delta(\omega_{\lambda} - \omega_{\lambda_1}). \tag{2.18}$$

The Kronecker deltas $\Delta_{\pm} = \Delta_{\mathbf{q}\pm\mathbf{q}_1-\mathbf{q}_2,\mathbf{R}}$ and $\Delta_{\pm\pm} = \Delta_{\mathbf{q}\pm\mathbf{q}_1\pm\mathbf{q}_2-\mathbf{q}_3,\mathbf{R}}$ describe the momentum selection rule. The delta function $\delta(\Delta\omega)$ in the calculation of each $\mathcal{L}$ can be evaluated by the Lorentzian function $(1/\pi)(\zeta/((\Delta\omega)^2 + \zeta^2))$. In the isotope scattering formula, $g_b = \sum_i f_{ib}(1 - m_{ib}/\bar{m}_b)^2$ measures the mass disorder, where i indicates isotope types, f_{ib} is the fraction of isotope i in lattice sites of basis atom b, m_{ib} is the mass of isotope i and $\bar{m}_b$ is the average atom mass of basis b sites. The transition probability matrices $V_{\pm}^{(3)}$ and $V_{\pm\pm}^{(4)}$ are

$$V_{\pm}^{(3)} = \sum_{b,l_1b_1,l_2b_2} \sum_{\alpha\alpha_1\alpha_2} \Phi_{0b,\ l_1b_1,\ l_2b_2}^{\alpha\alpha_1\alpha_2} \frac{\mathbf{e}_{\alpha b}^{\lambda} \mathbf{e}_{\alpha_1 b_1}^{\pm\lambda_1} \mathbf{e}_{\alpha_2 b_2}^{-\lambda_2}}{\sqrt{\bar{m}_b \bar{m}_{b_1} \bar{m}_{b_2}}} \mathrm{e}^{\pm i\mathbf{q}_1\cdot\mathbf{r}_{l_1} - i\mathbf{q}_2\cdot\mathbf{r}_{l_2}}, \tag{2.19}$$

$$V_{\pm\pm}^{(4)} = \sum_{b,l_1b_1,l_2b_2,l_3b_3} \sum_{\alpha\alpha_1\alpha_2\alpha_3} \Phi_{0b,\ l_1b_1,\ l_2b_2,\ l_3b_3}^{\alpha\alpha_1\alpha_2\alpha_3} \frac{\mathbf{e}_{\alpha b}^{\lambda} \mathbf{e}_{\alpha_1 b_1}^{\pm\lambda_1} \mathbf{e}_{\alpha_2 b_2}^{\pm\lambda_2} \mathbf{e}_{\alpha_3 b_3}^{-\lambda_3}}{\sqrt{\bar{m}_b \bar{m}_{b_1} \bar{m}_{b_2} \bar{m}_{b_3}}} \mathrm{e}^{\pm i\mathbf{q}_1\cdot\mathbf{r}_{l_1} \pm i\mathbf{q}_2\cdot\mathbf{r}_{l_2} - i\mathbf{q}_3\cdot\mathbf{r}_{l_3}}, \tag{2.20}$$

$\Phi_{0b,l_1b_1,l_2b_2}^{\alpha\alpha_1\alpha_2}$ and $\Phi_{0b,l_1b_1,l_2b_2,l_3b_3}^{\alpha\alpha_1\alpha_2\alpha_3}$ are the third-order and fourth-order IFCs.

Assume a perturbation in all the phonon modes [34, 41–43], we have

$$n_{\lambda} = n_{\lambda}^{0} + n_{\lambda}', \ n_{\lambda}' = -\Psi_{\lambda} \frac{\partial n_{\lambda}^{0}}{\partial(\hbar\omega_{\lambda})} = \Psi_{\lambda} \cdot \frac{1}{k_{\mathrm{B}}T} n_{\lambda}^{0}\left(n_{\lambda}^{0} + 1\right), \tag{2.21}$$

$$n_{\lambda_1} = n_{\lambda_1}^{0} + n_{\lambda_1}', \ n_{\lambda_1}' = -\Psi_{\lambda_1} \frac{\partial n_{\lambda_1}^{0}}{\partial(\hbar\omega_{\lambda_1})} = \Psi_{\lambda_1} \cdot \frac{1}{k_{\mathrm{B}}T} n_{\lambda_1}^{0}\left(n_{\lambda_1}^{0} + 1\right), \tag{2.22}$$

$$n_{\lambda_2} = n_{\lambda_2}^{0} + n_{\lambda_2}', \ n_{\lambda_2}' = -\Psi_{\lambda_2} \frac{\partial n_{\lambda_2}^{0}}{\partial(\hbar\omega_{\lambda_2})} = \Psi_{\lambda_2} \cdot \frac{1}{k_{\mathrm{B}}T} n_{\lambda_2}^{0}\left(n_{\lambda_2}^{0} + 1\right), \tag{2.23}$$

$$n_{\lambda_3} = n_{\lambda_3}^{0} + n_{\lambda_3}', \ n_{\lambda_3}' = -\Psi_{\lambda_3} \frac{\partial n_{\lambda_3}^{0}}{\partial(\hbar\omega_{\lambda_3})} = \Psi_{\lambda_3} \cdot \frac{1}{k_{\mathrm{B}}T} n_{\lambda_3}^{0}\left(n_{\lambda_3}^{0} + 1\right), \tag{2.24}$$

where Ψ measures the derivation in the phonon distribution from equilibrium, weighted with a factor that depends on the equilibrium distribution of that mode [34]. In the final step of each of equations (2.21)–(2.24), we used the fact that $\partial n^0/\partial(\hbar\omega) = -n^0(n^0 + 1)/k_{\mathrm{B}}T$. By substituting equations (2.21)–(2.24) into equation

(2.15) and dropping the higher-order terms $O(\Psi^2)$ and $O(\Psi^3)$, the scattering term of the linearized phonon BTE is written as

$$\begin{aligned}\left.\frac{\partial n'_\lambda}{\partial t}\right|_s = &-\sum_{\lambda_1\lambda_2}\frac{1}{k_\mathrm{B}T}\left\{\frac{1}{2}(\Psi_\lambda-\Psi_{\lambda_1}-\Psi_{\lambda_2})n_\lambda^0\left(1+n_{\lambda_1}^0\right)\left(1+n_{\lambda_2}^0\right)\mathcal{L}_-\right.\\ &\left.+(\Psi_\lambda+\Psi_{\lambda_1}-\Psi_{\lambda_2})n_\lambda^0 n_{\lambda_1}^0\left(1+n_{\lambda_2}^0\right)\mathcal{L}_+\right\}\\ &-\sum_{\lambda_1\lambda_2\lambda_3}\frac{1}{k_\mathrm{B}T}\left\{\frac{1}{6}(\Psi_\lambda-\Psi_{\lambda_1}-\Psi_{\lambda_2}-\Psi_{\lambda_3})\left(1+n_\lambda^0\right)n_{\lambda_1}^0 n_{\lambda_2}^0 n_{\lambda_3}^0\mathcal{L}_{--}\right.\\ &+\frac{1}{2}(\Psi_\lambda+\Psi_{\lambda_1}-\Psi_{\lambda_2}-\Psi_{\lambda_3})\left(1+n_\lambda^0\right)\left(1+n_{\lambda_1}^0\right)n_{\lambda_2}^0 n_{\lambda_3}^0\mathcal{L}_{+-}\\ &\left.+\frac{1}{2}(\Psi_\lambda+\Psi_{\lambda_1}+\Psi_{\lambda_2}-\Psi_{\lambda_3})\left(1+n_\lambda^0\right)\left(1+n_{\lambda_1}^0\right)\left(1+n_{\lambda_2}^0\right)n_{\lambda_3}^0\mathcal{L}_{++}\right\}\\ &-\sum_{\lambda_1}\frac{1}{k_\mathrm{B}T}(\Psi_\lambda-\Psi_{\lambda_1})n_\lambda^0\left(1+n_\lambda^0\right)\mathcal{L}_\mathrm{iso}-\frac{1}{k_\mathrm{B}T}\Psi_\lambda n_\lambda^0\left(1+n_\lambda^0\right)\frac{1}{\tau_{b,\lambda}^0}.\end{aligned} \tag{2.25}$$

Here, we have taken advantage of the identical relations

$$\lambda\to\lambda_1+\lambda_2\ :\ \ n_\lambda^0\left(1+n_{\lambda_1}^0\right)\left(1+n_{\lambda_2}^0\right)-\left(1+n_\lambda^0\right)n_{\lambda_1}^0 n_{\lambda_2}^0=0, \tag{2.26}$$

$$\lambda+\lambda_1\to\lambda_2\ :\ \ n_\lambda^0 n_{\lambda_1}^0\left(1+n_{\lambda_2}^0\right)-\left(1+n_\lambda^0\right)\left(1+n_{\lambda_1}^0\right)n_{\lambda_2}^0=0, \tag{2.27}$$

$$\lambda\to\lambda_1+\lambda_2+\lambda_3\ :\ \ n_\lambda^0\left(1+n_{\lambda_1}^0\right)\left(1+n_{\lambda_2}^0\right)\left(1+n_{\lambda_3}^0\right)-\left(1+n_\lambda^0\right)n_{\lambda_1}^0 n_{\lambda_2}^0 n_{\lambda_3}^0=0, \tag{2.28}$$

$$\lambda+\lambda_1\to\lambda_2+\lambda_3\ :\ \ n_\lambda^0 n_{\lambda_1}^0\left(1+n_{\lambda_2}^0\right)\left(1+n_{\lambda_3}^0\right)-\left(1+n_\lambda^0\right)\left(1+n_{\lambda_1}^0\right)n_{\lambda_2}^0 n_{\lambda_3}^0=0, \tag{2.29}$$

$$\lambda+\lambda_1+\lambda_2\to\lambda_3\ :\ \ n_\lambda^0 n_{\lambda_1}^0 n_{\lambda_2}^0\left(1+n_{\lambda_3}^0\right)-\left(1+n_\lambda^0\right)\left(1+n_{\lambda_1}^0\right)\left(1+n_{\lambda_2}^0\right)n_{\lambda_3}^0=0, \tag{2.30}$$

and

$$\begin{aligned}\lambda\to\lambda_1+\lambda_2\colon\left(1+n_{\lambda_1}^0\right)\left(1+n_{\lambda_2}^0\right)-n_{\lambda_1}^0 n_{\lambda_2}^0&=\frac{\left(1+n_{\lambda_1}^0\right)\left(1+n_{\lambda_2}^0\right)}{\left(1+n_\lambda^0\right)}\\ &=\frac{n_{\lambda_1}^0 n_{\lambda_2}^0}{n_\lambda^0}=1+n_{\lambda_1}^0+n_{\lambda_2}^0,\end{aligned} \tag{2.31}$$

$$\lambda + \lambda_1 \to \lambda_2\colon n^0_{\lambda_1}\left(1 + n^0_{\lambda_2}\right) - \left(1 + n^0_{\lambda_1}\right)n^0_{\lambda_2} = \frac{\left(1 + n^0_{\lambda_1}\right)n^0_{\lambda_2}}{n^0_\lambda} = \frac{n^0_{\lambda_1}\left(1 + n^0_{\lambda_2}\right)}{1 + n^0_\lambda} = n^0_{\lambda_1} - n^0_{\lambda_2}, \tag{2.32}$$

$$\lambda \to \lambda_1 + \lambda_2 + \lambda_3\colon \left(1 + n^0_{\lambda_1}\right)\left(1 + n^0_{\lambda_2}\right)\left(1 + n^0_{\lambda_3}\right) - n^0_{\lambda_1}n^0_{\lambda_2}n^0_{\lambda_3} = \frac{n^0_{\lambda_1}n^0_{\lambda_2}n^0_{\lambda_3}}{n^0_\lambda}, \tag{2.33}$$

$$\lambda + \lambda_1 \to \lambda_2 + \lambda_3\colon n^0_{\lambda_1}\left(1 + n^0_{\lambda_2}\right)\left(1 + n^0_{\lambda_3}\right) - \left(1 + n^0_{\lambda_1}\right)n^0_{\lambda_2}n^0_{\lambda_3} = \frac{\left(1 + n^0_{\lambda_1}\right)n^0_{\lambda_2}n^0_{\lambda_3}}{n^0_\lambda}, \tag{2.34}$$

$$\lambda + \lambda_1 + \lambda_2 \to \lambda_3\colon n^0_{\lambda_1}n^0_{\lambda_2}\left(1 + n^0_{\lambda_3}\right) - \left(1 + n^0_{\lambda_1}\right)\left(1 + n^0_{\lambda_2}\right)n^0_{\lambda_3} = \frac{\left(1 + n^0_{\lambda_1}\right)\left(1 + n^0_{\lambda_2}\right)n^0_{\lambda_3}}{n^0_\lambda}. \tag{2.35}$$

Equations (2.26–2.35) are obtained based on the energy conservation rule combined with the Bose–Einstein distribution. For example, equations (2.26) and (2.31) are derived by substituting ω of the Bose–Einstein distribution $e^{\hbar\omega/k_BT} = 1 + 1/n^0_\lambda$ into the energy conservation (selection rule) $\omega = \omega_1 + \omega_2$, giving the result $1 + 1/n^0_\lambda = (1 + 1/n^0_{\lambda_1})(1 + 1/n^0_{\lambda_2})$, which directly deduces equations (2.26) and (2.31).

The final expression of the right-hand side of the original phonon BTE (equation (2.2)) is obtained by defining the form [43] of

$$\Psi = -\hbar\omega\tau\mathbf{v}\cdot\nabla T/T \tag{2.36}$$

and putting it into equation (2.25) for all the modes λ, λ_1, λ_2 and λ_3, while the left-hand side of equation (2.2) is transformed by the identical relation

$$\frac{\partial n^0_\lambda}{\partial T} = \frac{1}{T}\frac{\hbar\omega_\lambda}{k_BT}n^0_\lambda\left(n^0_\lambda + 1\right). \tag{2.37}$$

Thus, the phonon BTE (equation (2.2)) is transformed as

$$
\begin{aligned}
1 = & \sum_{\lambda_1\lambda_2}\left\{\frac{1}{2}(\tau_\lambda - \tau_{\lambda_1}\xi_{\lambda\lambda_1} - \tau_{\lambda_2}\xi_{\lambda\lambda_2})\frac{\left(1+n^0_{\lambda_1}\right)\left(1+n^0_{\lambda_2}\right)}{1+n^0_\lambda}\mathcal{L}_- \right. \\
& \left. + (\tau_\lambda + \tau_{\lambda_1}\xi_{\lambda\lambda_1} - \tau_{\lambda_2}\xi_{\lambda\lambda_2})\frac{n^0_{\lambda_1}\left(1+n^0_{\lambda_2}\right)}{1+n^0_\lambda}\mathcal{L}_+\right\} \\
& + \sum_{\lambda_1\lambda_2\lambda_3}\left\{\frac{1}{6}(\tau_\lambda - \tau_{\lambda_1}\xi_{\lambda\lambda_1} - \tau_{\lambda_2}\xi_{\lambda\lambda_2} - \tau_{\lambda_3}\xi_{\lambda\lambda_3})\frac{n^0_{\lambda_1}n^0_{\lambda_2}n^0_{\lambda_3}}{n^0_\lambda}\mathcal{L}_{--}\right. \\
& + \frac{1}{2}(\tau_\lambda + \tau_{\lambda_1}\xi_{\lambda\lambda_1} - \tau_{\lambda_2}\xi_{\lambda\lambda_2} - \tau_{\lambda_3}\xi_{\lambda\lambda_3})\frac{\left(1+n^0_{\lambda_1}\right)n^0_{\lambda_2}n^0_{\lambda_3}}{n^0_\lambda}\mathcal{L}_{+-} \\
& \left. + \frac{1}{2}(\tau_\lambda + \tau_{\lambda_1}\xi_{\lambda\lambda_1} + \tau_{\lambda_2}\xi_{\lambda\lambda_2} - \tau_{\lambda_3}\xi_{\lambda\lambda_3})\frac{\left(1+n^0_{\lambda_1}\right)\left(1+n^0_{\lambda_2}\right)n^0_{\lambda_3}}{n^0_\lambda}\mathcal{L}_{++}\right\} \\
& + \sum_{\lambda_1}(\tau_\lambda - \tau_{\lambda_1}\xi_{\lambda\lambda_1})\mathcal{L}_{\text{iso}} + \frac{\tau_\lambda}{\tau^0_{b,\lambda}},
\end{aligned}
$$

and further as

$$
\tau_\lambda = \tau^0_\lambda(1 + \Xi_{3,\lambda} + \Xi_{4,\lambda} + \Xi_{\text{iso},\lambda}), \tag{2.38}
$$

with

$$
\frac{1}{\tau^0_\lambda} = \frac{1}{\tau^0_{3,\lambda}} + \frac{1}{\tau^0_{4,\lambda}} + \frac{1}{\tau^0_{\text{iso},\lambda}} + \frac{1}{\tau^0_{b,\lambda}}, \tag{2.39}
$$

$$
\frac{1}{\tau^0_{3,\lambda}} = \sum_{\lambda_1\lambda_2}\left\{\frac{1}{2}\left(1+n^0_{\lambda_1}+n^0_{\lambda_2}\right)\mathcal{L}_- + \left(n^0_{\lambda_1}-n^0_{\lambda_2}\right)\mathcal{L}_+\right\}, \tag{2.40}
$$

$$
\begin{aligned}
\frac{1}{\tau^0_{4,\lambda}} = & \sum_{\lambda_1\lambda_2\lambda_3}\left\{\frac{1}{6}\frac{n^0_{\lambda_1}n^0_{\lambda_2}n^0_{\lambda_3}}{n^0_\lambda}\mathcal{L}_{--} + \frac{1}{2}\frac{\left(1+n^0_{\lambda_1}\right)n^0_{\lambda_2}n^0_{\lambda_3}}{n^0_\lambda}\mathcal{L}_{+-}\right. \\
& \left. + \frac{1}{2}\frac{\left(1+n^0_{\lambda_1}\right)\left(1+n^0_{\lambda_2}\right)n^0_{\lambda_3}}{n^0_\lambda}\mathcal{L}_{++}\right\},
\end{aligned} \tag{2.41}
$$

$$
\frac{1}{\tau^0_{\text{iso},\lambda}} = \sum_{\lambda_1}\mathcal{L}_{\text{iso}}, \tag{2.42}
$$

$$
\frac{1}{\tau^0_{b,\lambda}} = \frac{2|v_{\lambda,x}|}{L} + \frac{2|v_{\lambda,y}|}{W}\frac{1-p}{1+p}. \tag{2.43}
$$

$$\Xi_{3,\lambda} = \sum_{\lambda_1\lambda_2} \left\{ \frac{1}{2}(\tau_{\lambda_1}\xi_{\lambda\lambda_1} + \tau_{\lambda_2}\xi_{\lambda\lambda_2})\left(1 + n^0_{\lambda_1} + n^0_{\lambda_2}\right)\mathcal{L}_{-} + (\tau_{\lambda_2}\xi_{\lambda\lambda_2} - \tau_{\lambda_1}\xi_{\lambda\lambda_1})\left(n^0_{\lambda_1} - n^0_{\lambda_2}\right)\mathcal{L}_{+} \right\}, \tag{2.44}$$

$$\Xi_{4,\lambda} = \sum_{\lambda_1\lambda_2\lambda_3} \left\{ \frac{1}{6}(\tau_{\lambda_1}\xi_{\lambda\lambda_1} + \tau_{\lambda_2}\xi_{\lambda\lambda_2} + \tau_{\lambda_3}\xi_{\lambda\lambda_3}) \frac{n^0_{\lambda_1} n^0_{\lambda_2} n^0_{\lambda_3}}{n^0_{\lambda}} \mathcal{L}_{--} + \frac{1}{2}(\tau_{\lambda_2}\xi_{\lambda\lambda_2} + \tau_{\lambda_3}\xi_{\lambda\lambda_3} - \tau_{\lambda_1}\xi_{\lambda\lambda_1}) \frac{\left(1 + n^0_{\lambda_1}\right) n^0_{\lambda_2} n^0_{\lambda_3}}{n^0_{\lambda}} \mathcal{L}_{+-} + \frac{1}{2}(\tau_{\lambda_3}\xi_{\lambda\lambda_3} - \tau_{\lambda_1}\xi_{\lambda\lambda_1} - \tau_{\lambda_2}\xi_{\lambda\lambda_2}) \frac{\left(1 + n^0_{\lambda_1}\right)\left(1 + n^0_{\lambda_2}\right) n^0_{\lambda_3}}{n^0_{\lambda}} \mathcal{L}_{++} \right\}, \tag{2.45}$$

$$\Xi_{\mathrm{iso},\lambda} = \sum_{\lambda_1} \tau_{\lambda_1}\xi_{\lambda\lambda_1}\mathcal{L}_{\mathrm{iso}}, \tag{2.46}$$

$$\xi_{\lambda\lambda_1} \equiv \frac{\omega_{\lambda_1}}{\omega_\lambda} \frac{\mathbf{v}_{\lambda_1} \cdot \nabla T}{\mathbf{v}_\lambda \cdot \nabla T} = \frac{\omega_{\lambda_1} v_{\lambda_1 x}}{\omega_\lambda v_{\lambda x}}, \tag{2.47}$$

$$\xi_{\lambda\lambda_2} \equiv \frac{\omega_{\lambda_2}}{\omega_\lambda} \frac{\mathbf{v}_{\lambda_2} \cdot \nabla T}{\mathbf{v}_\lambda \cdot \nabla T} = \frac{\omega_{\lambda_2} v_{\lambda_2 x}}{\omega_\lambda v_{\lambda x}}, \tag{2.48}$$

$$\xi_{\lambda\lambda_3} \equiv \frac{\omega_{\lambda_3}}{\omega_\lambda} \frac{\mathbf{v}_{\lambda_3} \cdot \nabla T}{\mathbf{v}_\lambda \cdot \nabla T} = \frac{\omega_{\lambda_3} v_{\lambda_3 x}}{\omega_\lambda v_{\lambda x}}. \tag{2.49}$$

In summary, τ_λ is obtained by solving equation (2.38), with equations (2.16)–(2.20) and (2.39)–(2.48). Since both the left- and right-hand sides contain the unknown τ_λ, equation (2.38) is solved iteratively and thus is also called the iterative scheme. τ^0_λ in equation (2.39) is the phonon relaxation time based on SMRTA [26]. In the boundary scattering term, L and W represent the length (along the heat flow direction) and the width (perpendicular to the heat flow direction) of the material. $0 \leqslant p \leqslant 1$ is the specularity parameter with $p = 0$ indicating an extremely rough surface and $p = 1$ indicating a mirror-like surface.

Generally, four-phonon scattering is dominated by the Umklapp processes and, therefore, the SMRTA τ^0_λ in equation (2.39) is accurate enough to account for the four-phonon scattering in general materials. In other words, to save time it is not necessary to take into account the iteration of $\Xi_{4,\lambda}$ in equation (2.38). However, in some materials such as graphene, the four-phonon scattering is dominated by normal processes, which lead to a collective behavior of phonons. In this case, $\Xi_{4,\lambda}$ cannot be neglected in the iteration in equation (2.38). Such a phenomenon results

from the fact that N-scattering itself does not contribute to thermal resistance since it conserves momentum.

Attention should be paid to the usage of eigenvectors **e** and the phases in the exponential terms in equations (2.19) and (2.20). In these equations, we assume that the eigenvectors are obtained by solving the dynamical matrix

$$D_{\alpha\alpha_1}^{bb_1}(\mathbf{q}) = \frac{1}{\sqrt{m_b m_{b_1}}} \sum_{l_1} \Phi_{0b,l_1b_1}^{\alpha\alpha_1} \mathrm{e}^{\mathrm{i}\mathbf{q}\cdot\mathbf{r}_{l_1}}, \tag{2.50}$$

which uses the positions of cells instead of atoms. However, if the eigenvectors are obtained by solving the dynamical matrix using

$$D_{\alpha\alpha_1}^{bb_1}(\mathbf{q}) = \frac{1}{\sqrt{m_b m_{b_1}}} \sum_{l_1} \Phi_{0b,l_1b_1}^{\alpha\alpha_1} \mathrm{e}^{\mathrm{i}\mathbf{q}\cdot(\mathbf{r}_{l_1b_1}-\mathbf{r}_{0b})}, \tag{2.51}$$

as implemented in Phonopy [44], one should use the positions of atoms ($\mathbf{r}_{lb}$) instead of the positions of cells ($\mathbf{r}_l$) in the phases of the exponential terms in equations (2.19) and (2.20), which should read

$$\mathrm{e}^{\pm\mathrm{i}\mathbf{q}_1\cdot\mathbf{r}_{l_1b_1}-\mathrm{i}\mathbf{q}_2\cdot\mathbf{r}_{l_2b_2}} \tag{2.52}$$

for three-phonon scattering and

$$\mathrm{e}^{\pm\mathrm{i}\mathbf{q}_1\cdot\mathbf{r}_{l_1b_1}\pm\mathrm{i}\mathbf{q}_2\cdot\mathbf{r}_{l_2b_2}-\mathrm{i}\mathbf{q}_3\cdot\mathbf{r}_{l_3b_3}} \tag{2.53}$$

for four-phonon scattering.

2.3 Strong four-phonon scattering potential

In this section, we demonstrate the significance of four-phonon scattering originating from strong scattering potential, i.e. strong anharmonicity. Figure 2.2 shows the sketches of the potential wells of weakly and strongly anharmonic materials. The exact potential energy is decomposed into the Tyler series to the second, third and fourth orders. The second-order expansion is harmonic and has large derivation from the exact potential. Since anharmonicity basically increases with increasing temperature, such derivation becomes large at high temperaures. The third-order (anharmonic) correction could alleviate such a derivation but is not adequate at high temperatures, while the fourth-order (anharmonic) correction brings the potential well much closer to exactly one. For weakly anharmonic materials, the fourth-order correction is negligible at low temperatures while it becomes significant at elevated temperatures. For strongly anharmonic materials, even starting from a low temperature, the fourth-order correction is large (while at high temperatures the fifth-order correction seems non-negligible). Note that 'high' or 'low' temperature is a relative quantity, depending on the Debye temperature (T_D) of a material. For example, 80 K is 'high' for solid argon ($T_D \approx 80$ K), while 300 K is 'low' for silicon ($T_D \approx 640$ K) and diamond ($T_D \approx 2220$ K).

Therefore, this section consists of two parts, demonstrating the two categories of materials with strong four-phonon scattering potential, i.e. weakly anharmonic

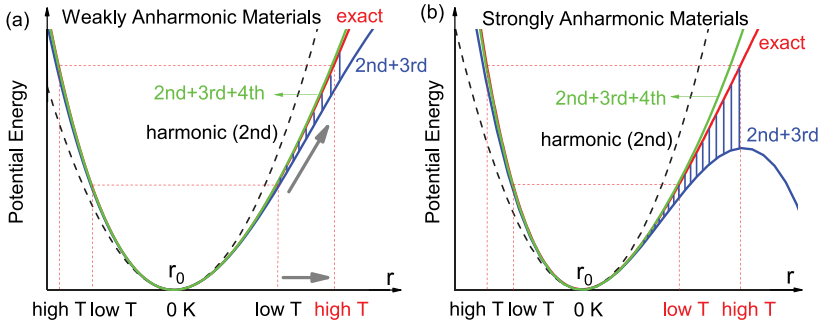

Figure 2.2. Sketches of the interatomic potentials of (a) weakly and (b) strongly anharmonic materials near the equilibrium position r_0. Shown are the exact potential (red solid curve), harmonic approximation (black dashed curve), third-order approximation (blue solid curve) and fourth-order approximation (green solid curve). The difference between the third-order approximation and the exact potential is marked by blue solid lines. The atomic vibration range is represented by temperature, i.e. atoms deviate from the equilibrium position more at higher temperatures. For weakly anharmonic materials, the fourth-order correction becomes important at elevated temperatures, while for strongly anharmonic materials, it is significant starting from low temperature.

materials at high temperatures (section 2.3.1) and strongly anharmonic materials even at low temperatures (section 2.3.2). For the first category, we take diamond, silicon and germanium as examples, which have high RT thermal conductivity. For the second category, we use solid argon, PbTe and NaCl as examples.

2.3.1 High temperature

The first category with strong four-phonon scattering potential is found in general solids at high temperatures, even with high RT thermal conductivity, such as diamond, silicon and germanium. As a starting point, classical potentials [45, 46] are used to calculate the fourth-order force constants as well as the four-phonon scattering rates [26]. The accuracy of four-phonon calculations is examined by comparing the thermal conductivities obtained from the three-/four-phonon scattering to those obtained from Green–Kubo MD simulations.

In figure 2.3, the three- and four-phonon scattering rates, $\tau_{3,\lambda}^{-1}$ and $\tau_{4,\lambda}^{-1}$, of diamond, Si and Ge are shown as a function of temperature. Far below their Debye temperatures, 2220, 640 and 374 K for diamond, Si and Ge, respectively, $\tau_{4,\lambda}^{-1}$ is generally negligible. However, $\tau_{4,\lambda}^{-1}$ increases faster than $\tau_{3,\lambda}^{-1}$ with increasing temperature and is no longer negligible when the temperature is high. Even for diamond, the most harmonic material with stiff bonds, it can be speculated from the trend that four-phonon scattering could be important when the temperature is close to its Debye temperature. We also noted that four-phonon scattering is relatively more important for optical phonons than acoustic phonons. This will be discussed in the following sections. The scaling laws $\tau_{3,\lambda}^{-1} \sim T$ and $\tau_{4,\lambda}^{-1} \sim T^2$ are found to be valid for both acoustic and optical phonons for all materials. These temperature dependences

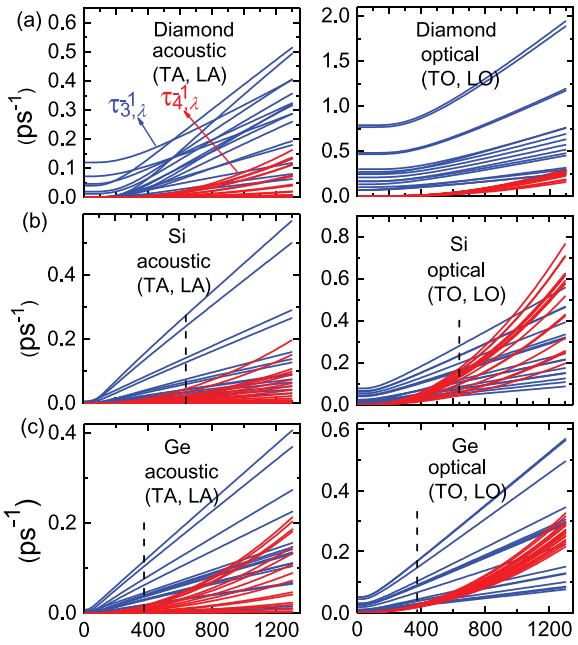

Figure 2.3. Temperature-dependent $\tau_{3,\lambda}^{-1}$ (blue) and $\tau_{4,\lambda}^{-1}$ (red) of the eight evenly sampled $\mathbf{q}$ points from Γ to X in diamond, silicon and germanium. Each curve represents an individual mode (a branch of a sampled $\mathbf{q}$ point). The dashed lines label Debye temperatures. The force constants are obtained from classical Tersoff potentials. Reproduced with permission from [26]. Copyright 2016 the American Physical Society.

result from equation (2.39), which roughly indicates $\tau_{3,\lambda}^{-1} \sim n^0$ and $\tau_{4,\lambda}^{-1} \sim (n^0)^2$, leading to $\tau_{3,\lambda}^{-1} \sim T$ and $\tau_{4,\lambda}^{-1} \sim T^2$ since n^0 is proportional to T at high temperatures.

The impact of four-phonon scattering on thermal conductivity is demonstrated by comparing

$$\kappa_{3,\mathrm{RTA},z} = \frac{1}{V}\sum_{\lambda} v_{z,\lambda}^2 c_\lambda \tau_{3,\lambda} \tag{2.54}$$

and

$$\kappa_{3+4,\mathrm{RTA},z} = \frac{1}{V}\sum_{\lambda} v_{z,\lambda}^2 c_\lambda \left(\tau_{3,\lambda}^{-1} + \tau_{4,\lambda}^{-1}\right)^{-1} \tag{2.55}$$

as shown in figures 2.4 and 2.8. For diamond, Si and Ge, κ_3 and κ_{3+4} match well with each other at low temperatures, indicating that four-phonon scattering is negligible. At room temperature, κ_{3+4} is lower than κ_3 by 1%, 8% and 15% for diamond, Si and Ge, respectively, as shown in the inset in figure 2.4. As the temperature increases to 1000 K, this discrepancy grows to 15%, 25% and 36%, respectively. Such results, again, indicate that even in weakly anharmonic materials, four-phonon scattering may play a critical role at high temperatures.

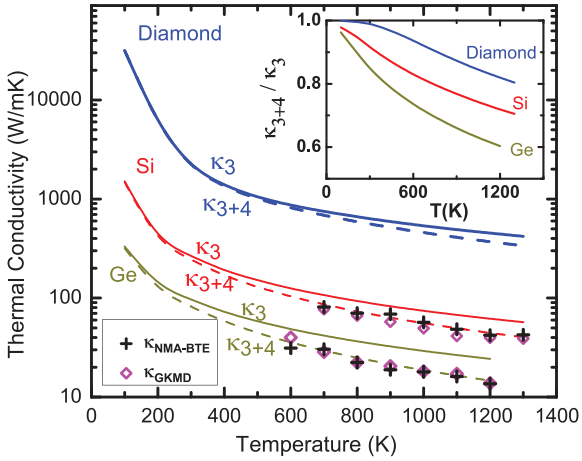

Figure 2.4. The comparison among $\kappa_{3,\mathrm{RTA}}$, $\kappa_{3+4,\mathrm{RTA}}$, $\kappa_{\mathrm{NMA,RTA}}$ and $\kappa_{\mathrm{Green-Kubo,RTA}}$ for diamond, silicon and germanium predicted from classical Tersoff potentials. The inset shows the ratio $\kappa_{3+4,\mathrm{RTA}}/\kappa_{3,\mathrm{RTA}}$. Reproduced with permission from [26]. Copyright 2016 the American Physical Society.

The accuracy of the four-phonon scattering calculation is examined by MD simulations, which naturally include all the orders of anharmonicities. κ_3 and κ_{3+4} are compared to κ_{NMA}, which is calculated by the BTE using the linewidth $\tau^{-1}_{\mathrm{NMA},\lambda}$ obtained from normal mode analysis (NMA) based on MD. They are also compared to $\kappa_{\mathrm{GK(MD)}}$ that is directly obtained from the Green–Kubo formalism based on MD. A good agreement between κ_{3+4} and κ_{NMA} as well as $\kappa_{\mathrm{GK(MD)}}$ is found for Si and Ge in figure 2.4. The comparison in diamond is not done since diamond has a high Debye temperature, below which κ_{3+4} obtained from quantum mechanics is not comparable to κ_{NMA} and $\kappa_{\mathrm{GK(MD)}}$ from classical MD. In contrast, κ_3 is considerably over-predicted, particularly at high temperatures. For clearer insight, we plot the ratio of κ_{3+4}/κ_3 as a function of temperature in the insets. Since we use empirical interatomic potentials that are approximations to the true atomic interactions, the numbers presented here should be understood with caution or on a semi-quantitative basis.

ALD and MD were regarded as two different methods. The phonon scattering rates calculated from the former and the phonon linewidths calculated from the latter were regarded as two separate quantities with their quantitative agreement remaining missing for a long time [25]. With the aid of four-phonon scattering, these two quantities match, and the two methods become consistent with each other. The four-phonon calculation pushes a step forward towards the 'unification' of the simulation methods of phonon and thermal transport.

To have a quantitative comparison between the four-phonon calculation and experiment, it is necessary to use DFT instead of empirical potentials for the calculation of force constants. The calculations were performed for diamond and silicon. While diamond will be shown in section 2.4.1 for special purposes, here we take silicon for demonstration. The three- and four-phonon scattering rates for all

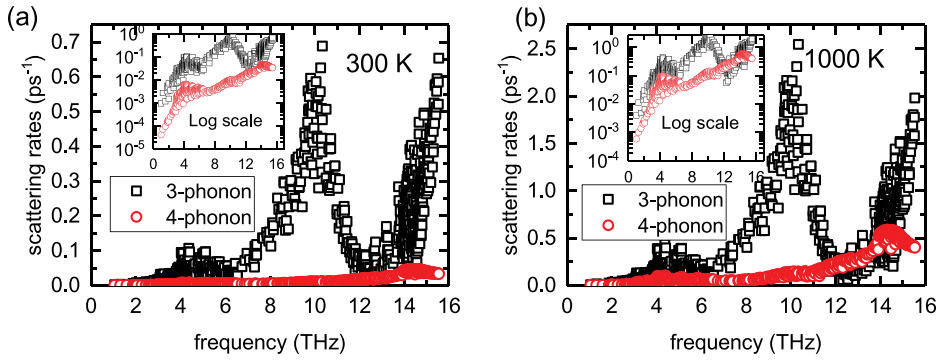

Figure 2.5. First-principles three-phonon (black squares) and four-phonon (red circles) scattering rates of Si at 300 and 1000 K with $16 \times 16 \times 16$ phonon **q** point grids. The insets are in log–linear scales to give a better view of the low-frequency regions. Reproduced with permission from [27]. Copyright 2017 the American Physical Society.

modes throughout the Brillouin zone of Si calculated from DFT are shown in figure 2.5 at 300 and 1000 K. The insets show the low-frequency behavior. We note that the four-phonon scattering rates increase quadratically with temperature, while three-phonon scattering rates increase linearly, not shown here. The trend is consistent with the preceding discussions based on classical potentials. At 300 K, τ_4^{-1} is well below τ_3^{-1} in Si throughout the frequency domain. As T increases to 1000 K, the four-phonon rates of the low-frequency phonons remain insubstantial; however, higher-energy longitudinal acoustic (LA) modes and all the optical modes exhibit large τ_4^{-1}, comparable to τ_3^{-1}. The large τ_4^{-1} of the heat-carrying LA phonons will have a substantial effect on the thermal conductivity of these materials, and that of the optical modes can affect infrared optical properties [19].

The thermal conductivity of silicon is calculated by solving the iterative phonon BTE beyond the RTA. Due to the high computational cost, the four-phonon scattering rates are computed at the RTA level only and inserted into the iterative scheme that determines the nonequilibrium phonon distributions from mixing of the three-phonon processes. This is similar to employing phonon–isotope and phonon–boundary scattering terms in the full BTE solution [9, 11, 47–51]. We will show that such an approximation is likely valid as the four-phonon scattering is dominated by Umklapp processes in section 2.5.2. We also include phonon–isotope scattering [37] in these κ calculations of naturally occurring materials. The iterative solution to the BTE for κ of the naturally occurring Si is shown in figure 2.6. The three-phonon predictions agree well with measured data at low temperature (<600 K); however, significant deviations from experiment occur at high temperatures. For example, at 1000 K three-phonon resistance alone over-predicts the measured κ of silicon by 26%. In section 2.4.1, we will see that the over-prediction is also around 30% for diamond at 1000 K. Four-phonon scattering eliminates such discrepancies and brings the prediction to match well with experimental values. These examples demonstrate the significance of four-phonon scattering due to a strong scattering potential at high temperatures.

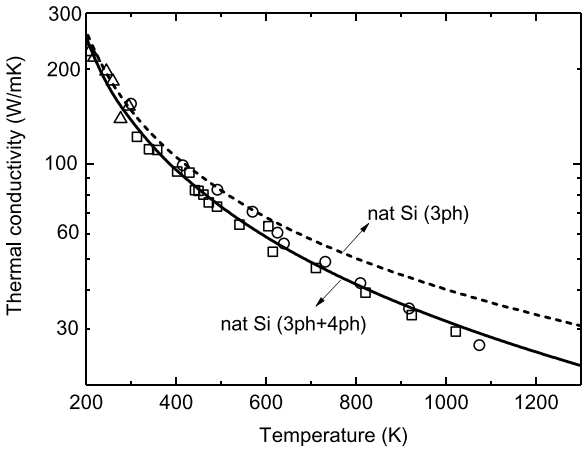

Figure 2.6. Thermal conductivities of naturally occurring Si. Dashed lines give first-principles calculated κ_3, while solid lines give κ_{3+4}. Calculation data are taken from [27]. Symbols represent measured data from: [52] triangles; [53] squares; and [54] circles.

2.3.2 Strongly anharmonic materials

For materials with low thermal conductivity, the four-phonon scattering potential is high even at ordinary temperature. We take Lennard-Jones argon as the benchmark material and then move onto more practically important materials, PbTe and NaCl. The scattering rates and thermal conductivity of argon are shown in figures 2.7 and 2.8, respectively. The summation of three- and four-phonon rates $\tau_{3,\lambda}^{-1} + \tau_{4,\lambda}^{-1}$ agrees well with MD results, $\tau_{\mathrm{NMA},\lambda}^{-1}$. It is seen that four-phonon is non-negligible even far below its Debye temperature and that it reduces the κ of argon by 35%–65% from 20 to 80 K.

PbTe and NaCl are two strongly anharmonic materials, in which the four-phonon scattering potential is high even at RT [32, 33]. It is also found that for those materials the phonon frequency shift at finite temperature is large and would affect the phonon scattering rates. Phonon modes at finite temperature are softened by anharmonicity via anharmonic three- and four-phonon scatterings as well as thermal expansion [55]. The phonon scattering, phonon frequency and thermal expansion are coupled together. Phonon scattering affects thermal expansion and changes phonon frequency, while thermal expansion also shifts phonon frequency, which in turn affects phonon scattering.

Strongly anharmonic materials generally have strong four-phonon scattering and, at the same time, their phonon frequencies at finite temperatures shift considerably away from those at 0 K due to the strong anharmonicity, which typically induces large thermal expansion as well as bond softening. The steps to reasonably include most anharmonic effects for thermal conductivity prediction with the current computational power are described in [32, 33] and are briefly summarized as follows. Step 1: Determine the correct temperature-dependent lattice constant, i.e. thermal expansion coefficient, by using quasiharmonic approximation (QHA)

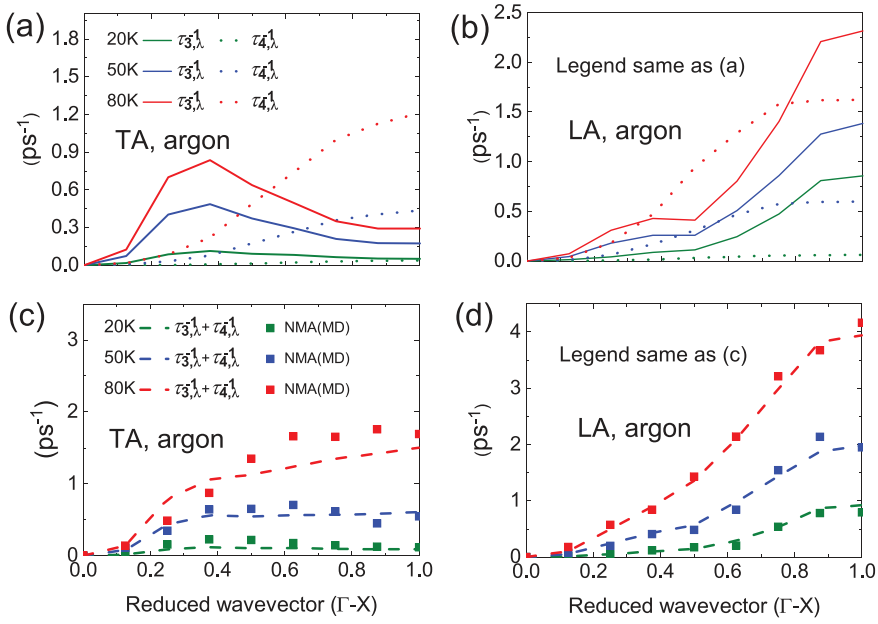

Figure 2.7. (a) and (b) A comparison between three- and four-phonon scattering rates for Lennard-Jones argon. (c) and (d) The total scattering rates ($\tau_{3,\lambda}^{-1} + \tau_{4,\lambda}^{-1}$) compared to the linewidths obtained from NMA based on MD simulations. Reproduced with permission from [26]. Copyright 2016 the American Physical Society.

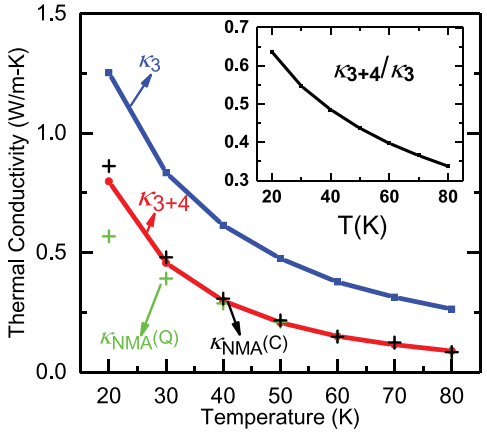

Figure 2.8. The κ values of Lennard-Jones argon predicted from $\tau_{3,\lambda}^{-1}$, $\tau_{3,\lambda}^{-1} + \tau_{4,\lambda}^{-1}$ and $\tau_{\mathrm{NMA},\lambda}^{-1}$ as a function of temperature, with the inset showing the ratio of κ_{3+4}/κ_3. κ_{NMA}(Q) and κ_{NMA}(C) represent that the specific heat is calculated by the quantum (Bose–Einstein) and classical (Boltzmann) phonon distributions, respectively. The phonon dispersion used in the calculation of κ_{NMA} is from lattice dynamics (LD) calculation at 0 K, to be consistent with the κ_3 and κ_{3+4} calculations. Reproduced with permission from [26]. Copyright 2016 the American Physical Society.

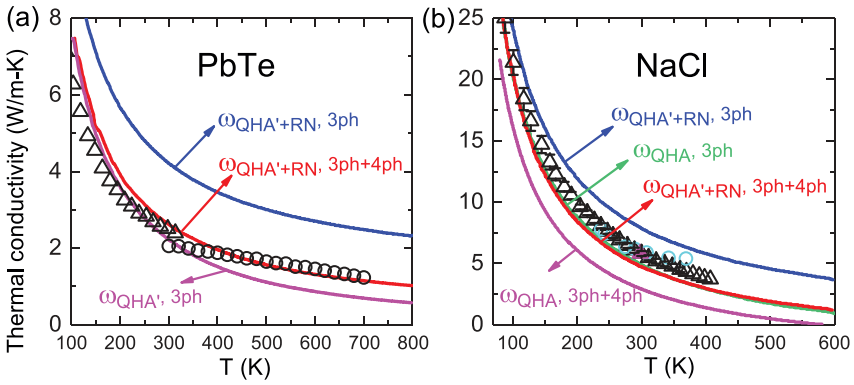

Figure 2.9. The thermal conductivities of PbTe and NaCl calculated from DFT (solid curves) in comparison to experimental data (symbols). First-principles data are taken from [32] for PbTe and [33] for NaCl. The experimental data are taken from [56, 57] for PbTe and [58–60] for NaCl.

together with phonon renormalization (RN), hereafter referred to as QHA′. Step 2: Determine the harmonic phonon frequency $\omega_{\mathrm{QHA}'}$ at the temperature-dependent lattice constant for a given temperature. Step 3: Calculate the anharmonic frequency $\omega_{\mathrm{QHA}'+\mathrm{RN}}$ by taking into account phonon renormalization. Step 4: Calculate the three- and four-phonon scattering rates as well as thermal conductivity based on the anharmonic frequency $\omega_{\mathrm{QHA}'+\mathrm{RN}}$. Steps 3 and 4 could be performed at the same time by calculating the real and imaginary parts of the phonon self-energy [2, 26, 32, 55] to avoid the double counting of phonon anharmonicity.

Figure 2.9 shows the thermal conductivities of PbTe and NaCl calculated by considering different degrees of anharmonicity as compared to experimental values. It is found that the three-phonon scattering without phonon renormalization can somehow predict the thermal conductivities well. After the phonon renormalization is included, the predicted thermal conductivities appear far above experimental values. If four-phonon scattering is considered, it pulls back the thermal conductivity prediction to agree well with experiments. Therefore, the agreement between the prediction and experimental values achieved by three-phonon scattering calculations without phonon renormalization or four-phonon scattering is a coincidence. The reason is that phonon renormalization largely shrinks the phonon scattering phase space while the inclusion of four-phonon scattering increases the scattering phase space, and they cancel each other for PbTe and NaCl. When the phonon renormalization effect and the four-phonon scattering are both considered, the thermal conductivity prediction reaches the best accuracy. At this moment, it is still an open question whether this phenomenon appears in PbTe and NaCl only or in a broader scope of strongly anharmonic materials.

2.4 Large four-phonon or suppressed three-phonon phase space

Apart from a strong scattering potential, the other origin of strong four-phonon scattering is the large scattering phase space. In this section, we will discuss such groups of materials, including the materials with large acoustic–optical phonon

band gaps and two-dimensional materials with reflection symmetry. We will also particularly discuss optical phonon modes, which usually have a large density of states and, therefore, large four-phonon scattering phase space.

2.4.1 Materials with large acoustic–optical phonon band gaps

When a material is composed of two elements with a large atomic mass ratio, the phonon vibration spectrum often presents a band gap. For example, the III–V or IV–IV binary zinc-blende BAs, SiC, AlAs, AlSb, GaN, GaP, InAs and InP all show a band gap, as shown in figure 2.10. Lindsay *et al* [11] found that phonon band gaps limited the three-phonon scattering phase space since the energy summation of two lower-branch phonons could hardly reach the high energy of optical phonon branches. As a result, the thermal conductivity predicted by three-phonon scattering

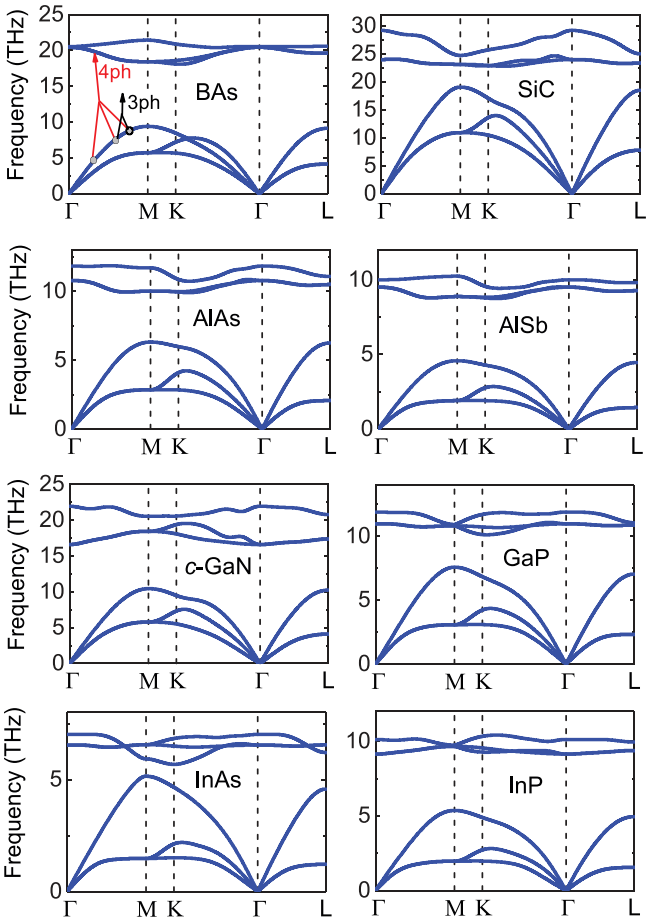

Figure 2.10. First-principles phonon dispersion of III–V binary compounds with phonon band gaps, which limit three-phonon processes but limit four-phonon processes less. Data from [20]. These dispersion relations agree well with experiment, as seen in [20].

for these materials is often very high. However, Feng *et al* [27] found that such band gaps do not restrict four-phonon scattering significantly since three lower-branch phonons are easily combined into a high-branch phonon mode, allowed by the energy conservation law, as shown in figure 2.10. As a consequence, four-phonon scattering in these materials is of significance to their thermal conductivity predictions.

A predominant example is BAs, which has been predicted using three-phonon scattering to own a thermal conductivity of 2 200 W (m K)$^{-1}$ at room temperature [11], being comparable to diamond, the highest in nature. Given such high thermal conductivity, it potentially opens an opportunity for thermal management of electronic devices.

However, Feng *et al* [27] found that four-phonon scattering is strong in BAs. In figure 2.11, the first-principles three- and four-phonon scattering rates of BAs are compared to those of diamond. The relative importance of four-phonon scattering in these two materials shows a clear difference. At room temperature, diamond shows negligible τ_4^{-1} throughout the whole spectrum, while BAs present non-negligible τ_4^{-1} for higher-branch acoustic phonons as well as all optical phonons. For example, three-phonon scattering rates have a deep valley at around 21 THz, i.e. for the optical phonon at the Γ point. These modes with high energy and small

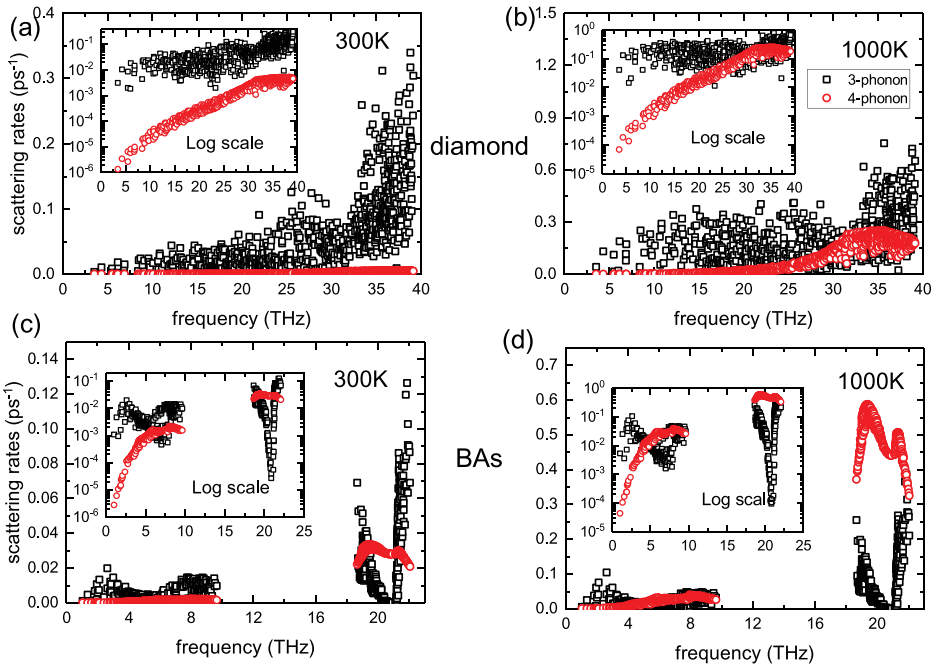

Figure 2.11. First-principles three-phonon (black squares) and four-phonon (red circles) scattering rates of diamond and BAs at 300 and 1000 K with 16 × 16 × 16 phonon **q** point grids. The insets are in log–linear scale to give a better view of the low-frequency regions. Reproduced with permission from [27]. Copyright 2017 the American Physical Society.

momentum can hardly find two other phonon modes that satisfy energy conservation and momentum conservation simultaneously. Such a large phonon band gap, however, does not forbid three acoustic phonons from combining into an optical mode. The predicted thermal conductivity of BAs after including four-phonon scattering at room temperature is reduced significantly, from ~2200 W(m K)$^{-1}$ to ~1400 W (m K)$^{-1}$, as shown in figure 2.12. Such reduction grows with increasing temperature, and the temperature-scaling trend at elevated T changes from $\kappa_3 \sim T^{-0.84}$ to $\kappa_{34} \sim T^{-1.64}$.

In 2018, several experimental works [28–30] grew high-purity BAs single crystals and verified the predicted thermal conductivity of BAs by including four-phonon scattering. As shown in figure 2.12, both the thermal conductivity values and temperature dependence measured from experiments agree well with the predictions. Without four-phonon scattering, one can fit the thermal conductivity to match the experiment at a certain temperature by adding phonon–defect scattering [29], which, however, cannot reproduce a correct temperature-scaling trend. Therefore, it is safe to conclude that the lower thermal conductivity of experimental samples compared to κ_3 is due to the strong four-phonon scattering, rather than defects. Later, the four-phonon scattering in boron phosphide (BP) was also verified in an experiment by Cahill *et al* [65].

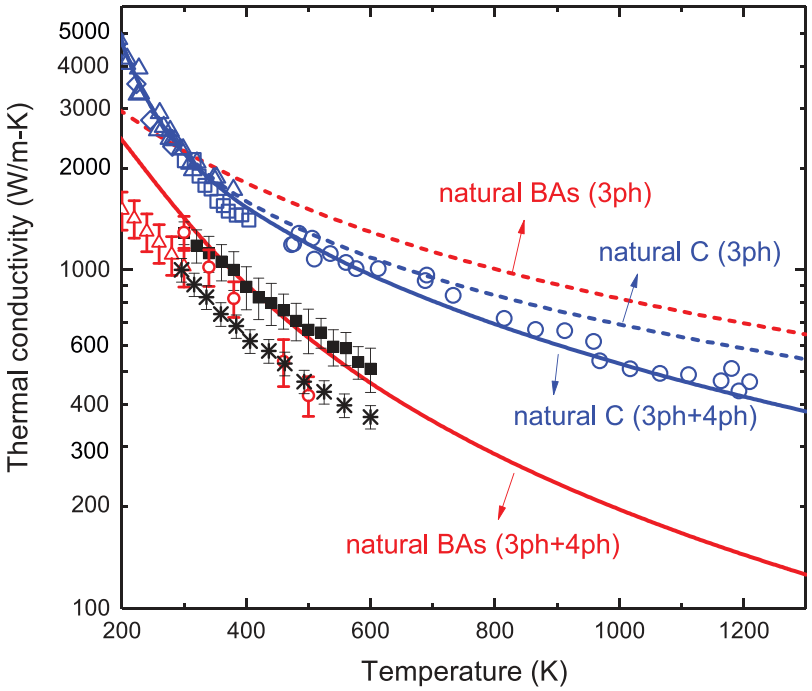

Figure 2.12. Thermal conductivities of naturally occurring diamond and BAs. Dashed lines give calculated κ_3, while solid lines give κ_{3+4}. First-principles data (curves) are taken from [27]. The symbols represent measured data. For diamond: blue triangles [61], blue squares [62], blue circles [63], blue squares [64]; for BAs: black squares [29], black stars [30], red circles [28] and red triangles [28].

In diamond, which does not present a phonon band gap, four-phonon scattering is not as strong as in BAs but is certainly not negligible at high temperatures. As T increases to 1000 K, four-phonon rates of the low-frequency phonons remain insubstantial, however, higher-energy LA modes and all the optical modes exhibit large τ_4^{-1}, comparable to τ_3^{-1} leading to a 23% reduction to the thermal conductivity.

The other materials with phonon band gaps may also show a large reduction of thermal conductivity with four-phonon scattering. Figure 2.13 shows another example, cubic GaN (*c*-GaN), in which the four-phonon scattering brings the thermal conductivity prediction down by a considerable amount to agree well with experiment.

Yang *et al* [66] found that for some materials in which optical branches have long three-phonon lifetimes, e.g. AlSb, four-phonon scattering is even more critical than three-phonon scattering as it diminishes optical phonon thermal transport, and therefore significantly reduces the thermal conductivities. Also, they showed that four-phonon scattering can play an extremely important role in weakening the isotope effect on κ. Specifically, four-phonon scattering reduces the room-temperature κ of the isotopically pure and naturally occurring AlSb by 70% and 50%, respectively (figure 2.14). The reduction for isotopically pure and naturally occurring *c*-GaN is about 34% and 27%, respectively. For isotopically pure wurtzite GaN (*w*-GaN), the reduction is about 13% at room temperature and 25% at 400 K. These results provided important guidance for experimentalists for achieving high thermal conductivities in III–V compounds for applications in semiconductor industry.

2.4.2 Optical phonons

The linewidths of infrared-active zone-center phonons are also important for the infrared dielectric functions of polar materials, which are key for applications in sensing, radiative cooling, energy harvesting, metamaterials, etc. For example, in polar compound semiconductors such as BAs, BN and SiC crystals, the zone-center longitudinal optical (LO) phonon lifetime plays an essential role in mediating the

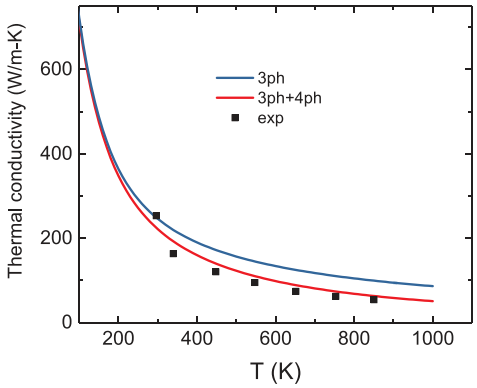

Figure 2.13. Thermal conductivity of *c*-GaN. First-principles data (solid curves) are taken from [66]. The experiment values (black squares) are taken from [67].

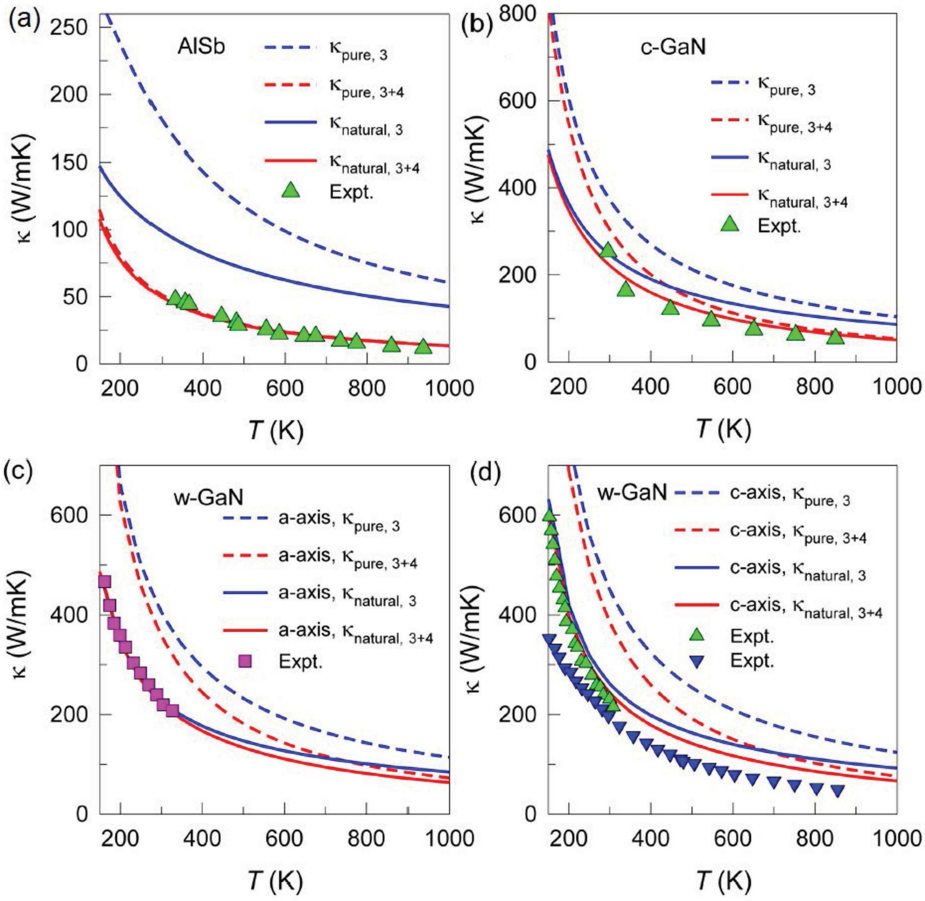

Figure 2.14. Lattice thermal conductivity as a function of temperature for (a) AlSb, (b) cubic GaN and wurtzite GaN along the (c) in-plane and (d) through-plane directions. Dashed lines represent the calculated isotopically pure κ_{pure} and solid lines represent the calculated naturally occurring $\kappa_{natural}$. The blue lines give the calculated κ with only three-phonon scattering and red lines give the results after including four-phonon scattering. All symbols represent experimental data for naturally occurring materials, which can be found in [66].

energy exchanges between the hot electrons and the lattice through Fröhlich interaction [68]. The materials such as GaN, GaAs and AlAs are promising candidates for use in optoelectronic devices and electronics. In addition, optical phonon scattering is also crucial to the thermal conductivity of certain materials that have a large number of optical phonon branches.

Optical phonons often exhibit relatively stronger four-phonon scattering compared to acoustic phonons as shown in the preceding sections. The reason is that optical phonons typically have a much higher density of states. Such a large amount of modes crowded within a narrow frequency range enabled large four-phonon scattering phase space for the process $\lambda_1 + \lambda_2 \rightarrow \lambda_3 + \lambda_4$ with $\lambda_{1,2,3,4}$ having similar

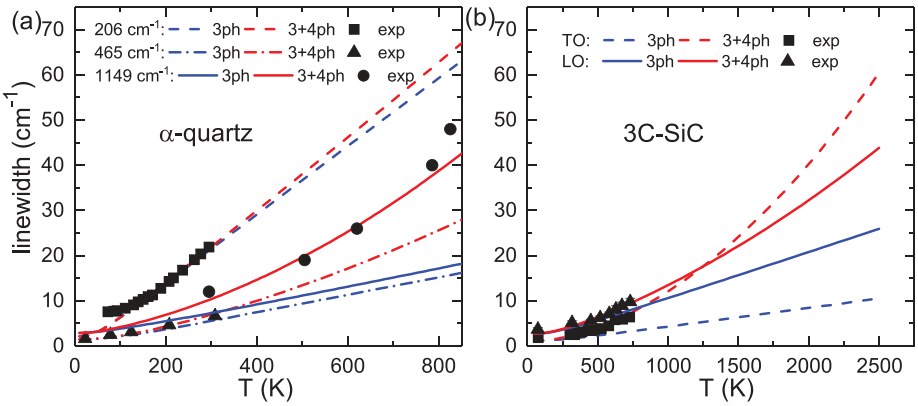

Figure 2.15. The optical phonon linewidth at the Γ point for α-quartz and 3*C*-SiC. First-principles data from [20]. Experimental data from [69, 70] for α-quartz and [16, 71] for SiC.

energy. More importantly, for the materials with phonon band gaps, four-phonon scattering is exceptionally important.

Figure 2.15 shows the zone-center optical phonon linewidths of α-quartz and 3*C*-SiC [20]. Figure 2.16 shows those of III–V compounds including *c*-BN, BAs, AlP, AlAs, AlSb, *c*-GaN, GaP, GaAs, GaSb, InP, InAs and InSb [20]. The first-principles calculated linewidths without four-phonon scattering are compared to available experimental values. The predicted optical phonon linewidths with only three-phonon scattering significantly disagree with the Raman measurements at mid and high temperatures. With four-phonon scattering included, reasonable agreements with available experimental data are achieved, demonstrating the significance of four-phonon processes in determining their infrared phonon linewidths.

For BAs in particular, it can be seen that the three-phonon processes have no contribution to optical phonon linewidth. This is due to the large acoustic–optical (a–o) gap as discussed in the preceding section. A similar case is also found in AlSb.

Note that for *c*-BN, BAs, InAs and InSb, even including four-phonon scattering, the prediction still has a significant discrepancy with experiments at higher temperatures, reflecting that five-phonon and higher-order phonon scattering may not be negligible in these particular materials.

To understand the high τ_4^{-1} of optical phonons, we show the contributions of different four-phonon processes of AlAs as an example in figure 2.17 (a). Clearly, it shows that the redistribution process $\lambda_1 + \lambda_2 \rightarrow \lambda_3 + \lambda_4$ dominates the four-phonon scattering of the optical phonon mode. This can be understood since the redistribution process is largely facilitated by the crowded branches of the optical phonon modes, as shown in figure 2.17 (b), among which the conservation law of energy and momentum can easily be satisfied by the four-phonon redistribution process. Actually, this is a general phenomenon since optical branches are bunched closely in energy in general materials, not limited to those with large acoustic–optical band gaps. This could also be the reason why optical phonons generally have strong four- and even higher-order phonon scattering.

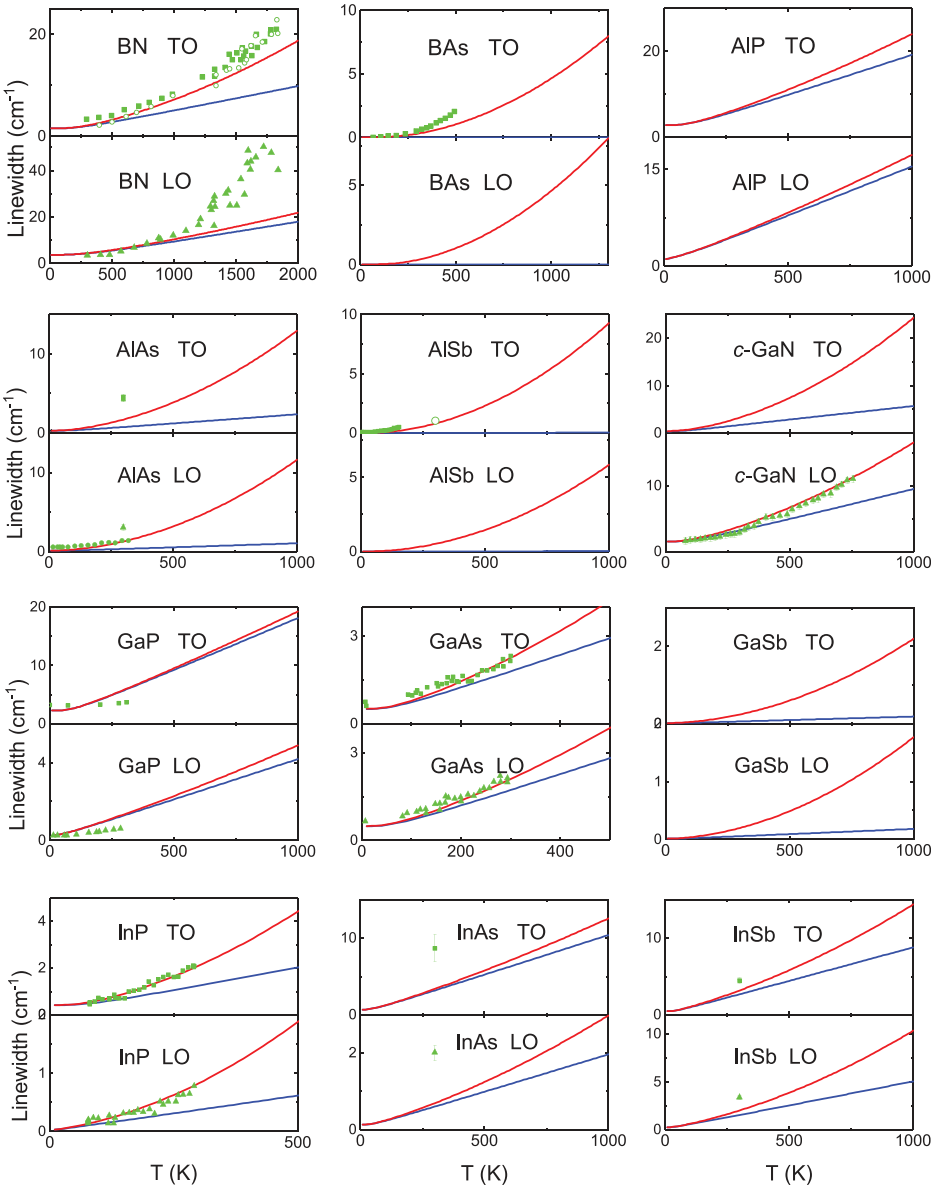

Figure 2.16. The optical phonon linewidth at the Γ point for group III–V zinc-blende compounds. First-principles data: τ_3^{-1} (blue curves) and $\tau_3^{-1} + \tau_4^{-1}$ (red curves) are taken from [20]. Note that the isotope or defect scattering is not included in the theoretical data here. Experimental values (green dots): *c*-BN [72], BAs [73], AlAs [74], AlSb [75, 76], *c*-GaN [77], GaP [6], GaAs [78], InP [78], InAs [79, 80] and InSb [75, 76].

The impact on optical phonon linewidth can also significantly affect thermal transport. For example, the three-phonon scattering predicts that the RT thermal conductivity of AlSb is about 98.8 W (m K)$^{-1}$, in which optical phonons contribute 49% [66]. However, after the four-phonon scattering is included, the RT κ is reduced

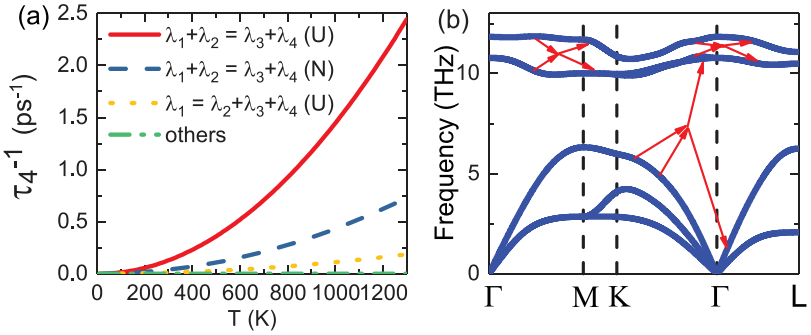

Figure 2.17. (a) First-principles scattering rates of the TO mode of AlAs from different four-phonon processes. (b) Sketch of the redistribution processes $\lambda_1 + \lambda_2 \rightarrow \lambda_3 + \lambda_4$. Data from [20].

to 39.5 W(m K)$^{-1}$ and the contribution of optical phonons is reduced to about 4%, that is, four-phonon scattering nearly kills the thermal transport of optical phonons in AlSb [66]. At 1000 K, the reduction is even larger, from 64% to 2%.

2.4.3 Two-dimensional materials with reflection symmetry

Two-dimensional materials with reflection symmetry are another example in which three-phonon scattering is largely limited [81, 82], leaving four-phonon scattering plenty of room to make a significant difference [31]. Graphene and hexagonal BN are two examples that have been demonstrated by Lindsay *et al* to have reflection symmetry [81, 82]. In this section, we take graphene as an example to demonstrate the possible role of four-phonon scattering.

Graphene has attracted intense interest for both fundamental research and practical applications due to its unique structure and extraordinary properties. The two-dimensional honeycomb structure, the zero band gap and the strong sp^2 bond endow graphene with unique electronic, thermal, optical and mechanical behaviors. The thermal transport in graphene has been quite intriguing since it was discovered that the scattering of flexural (out-of-plane) modes is largely forbidden by the reflection symmetry, leading to long relaxation times and high thermal conductivity. Three-phonon scattering theory predicts the room-temperature thermal conductivity of single-layer graphene as being around 3000 W (m K)$^{-1}$ [83, 84]. Different experimental methods, conditions and samples, however, showed quite different thermal conductivity values ranging from ~1500 to ~4000 W (m K)$^{-1}$ [85–89], and the widely used Raman technique has been questioned for use on graphene recently [90], leaving the thermal conductivity value of graphene even more mysterious.

Reflection symmetry in 2D materials forbids all the phonon–phonon scattering processes that involve an odd number of flexural modes [82]. Lindsay *et al* found numerically that in graphene the three-phonon scattering rates of the processes that involve 1 or 3 flexural modes are zero [82]. Feng and Ruan have verified numerically that the four-phonon scattering rates of the processes that involve 1 or 3 flexural modes are zero as well. Therefore, three-phonon processes can only involve 0 or 2

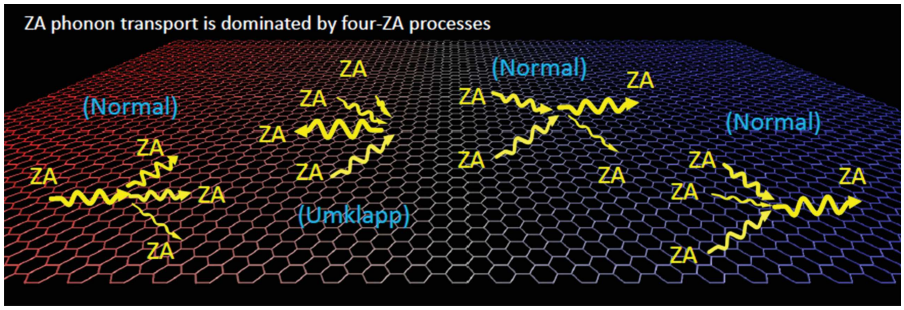

Figure 2.18. The 4-ZA processes in SLG. Reproduced with permission from [31]. Copyright 2018 the American Physical Society.

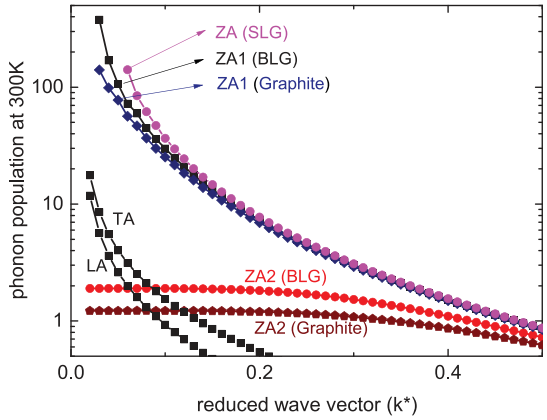

Figure 2.19. The phonon populations for different branches in SLG, bilayer graphene (BLG) and graphite. Data from [31].

flexural modes, while the four-phonon processes may involve 0, 2 or 4 flexural modes. Feng and Ruan found that most (60%–90%) of the three-phonon scattering processes of the ZA branch are forbidden by the reflection symmetry, while only about 40% of four-phonon scattering processes of the ZA branch are forbidden. Most importantly, four-phonon scattering allows two important processes, ZA + ZA → ZA + ZA and ZA ↔ ZA + ZA + ZA, which are called 4-ZA processes, shown in figure 2.18. Due to the quadratic dispersion relation, the ZA mode has quite a high phonon population near the Γ point as shown in figure 2.19. Therefore, these processes have ultra-high scattering rates since the four-phonon scattering is roughly proportional to the square of the phonon population.

The SMRTA-based three- and four-phonon scattering rates obtained from optimized Tersoff potential are compared in figure 2.20 [31]. Since the scattering rates follow the temperature dependence of $1/\tau^0_{3,\lambda} \sim T$ and $1/\tau^0_{4,\lambda} \sim T^2$, similarly to those in bulk materials [26, 27], we take the temperatures at 300 and 700 K as examples to show the amplitudes of $1/\tau^0_{3,\lambda}$ and $1/\tau^0_{4,\lambda}$ as a function of the reduced wave vector from Γ to M. We find that $1/\tau^0_{4,\lambda}$ is comparable to or even much higher than

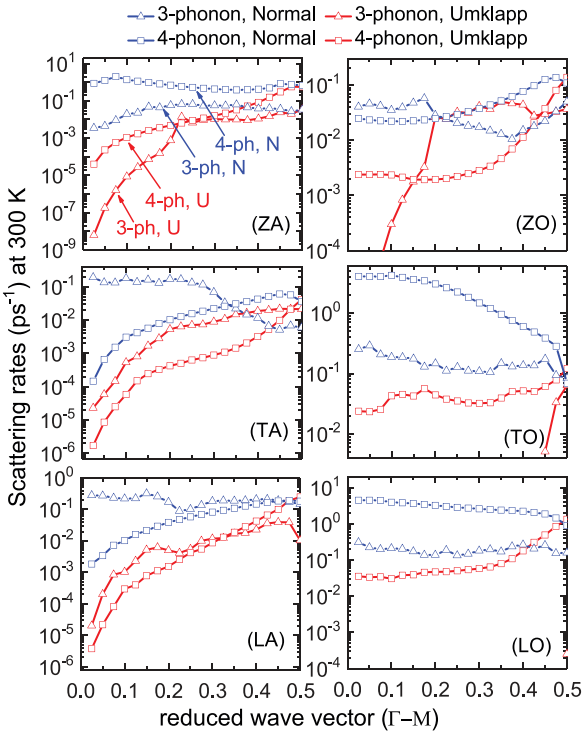

Figure 2.20. The three-phonon and four-phonon scattering rates, $\tau_{3(N)}^{-1}$, $\tau_{3(U)}^{-1}$, $\tau_{4(N)}^{-1}$ and $\tau_{4(U)}^{-1}$, of the six branches of SLG with respect to the reduced wave vector (Γ–*M*) at 300 K calculated by using the optimized Tersoff potential. Data from [31].

$1/\tau_{3,\lambda}^{0}$, even at room temperature, in particular for the ZA, TO and LO branches. For instance, $1/\tau_{3,\lambda}^{0}$ of the ZA branch at room temperature is typically below 0.08 ps^{-1} while the value of $1/\tau_{4,\lambda}^{0}$ is about 0.42-2 ps^{-1}, which indicates the relaxation time of ZA mode at room temperature is about 0.5–2 ps, far below expectations. At 700 K, the $1/\tau_{4,\lambda}^{0}$ of the ZA, TO and LO branches even reach above 10 ps^{-1}, being 2–3 orders higher than $1/\tau_{3,\lambda}^{0}$.

Feng and Ruan [31] found that the ZA four-phonon scattering is dominated by the normal (N) process, as shown in figure 2.20, indicating hydrodynamic behavior of phonon transport. Therefore, the SMRTA is not accurate to calculate the thermal conductivity, instead, the iterative solution to the BTE is needed. Feng and Ruan solved the iterative solution of BTE by including both three- and four-phonon scatterings, and they showed that the thermal conductivity of 9 μm graphene is reduced significantly from ~3383 to ~810 W(m K)$^{-1}$ after including the four-phonon scattering [31] (figure 2.21). Later in 2019, Gu *et al* refined the calculation of four-phonon scattering in single-layer graphene by using a smeared broadening factor as well as a temperature-dependent phonon dispersion relation [91]. They further confirmed the striking importance of four-phonon scattering in SLG and found that the thermal conductivity, using the optimized Tersoff potential, is about

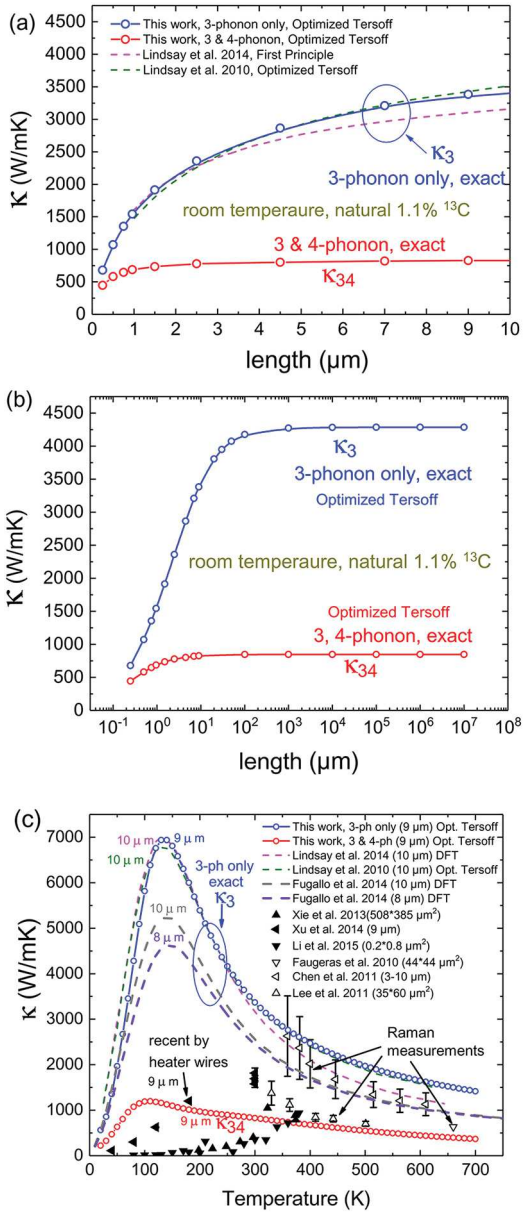

Figure 2.21. (a) Length-dependent thermal conductivity of single-layer graphene at 300 K. (b) Length convergence of thermal conductivity at 300 K. (c) Temperature-dependent lattice thermal conductivity. The dashed lines represent the theoretical predictions from the literature with three-phonon scattering only. The solid lines with open circles that are marked 'this work' are the predictions from [31]. In all the predictions, the natural 1.1% ^{13}C is included with the exact solution to the linearized BTE. The triangles show the experimental measured results. Data from Lindsay *et al* [82, 83], Fugallo *et al* [84], Xie *et al* [93], Xu *et al* [87], Li *et al* [94], Faugeras *et al* [85], Chen *et al* [95] and Lee *et al* [96]. Reproduced with permission from [31]. Copyright 2018 the American Physical Society.

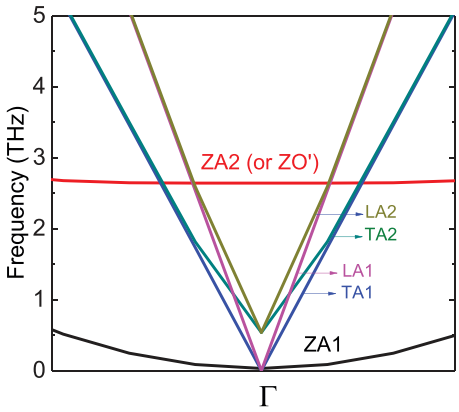

Figure 2.22. The phonon dispersion near the zone center along Γ–*M* in bilayer graphene calculated using an optimized Tersoff potential.

1900 W(m K)$^{-1}$. Since the fourth-order force constant of the classical interatomic potential [92] has not been validated against first-principles, the absolute values of the thermal conductivity after including four-phonon scattering should be interpreted qualitatively.

Since the four-phonon scattering rates in SLG are high, two natural questions are: (i) Does four-phonon scattering play an important role in multilayer graphene and graphite? (ii) Is five-phonon scattering important in SLG? The answers are negative for both questions. To address the first question, we plot the phonon dispersion of bilayer graphene in figure 2.22. Due to the interlayer van der Waals interaction, the ZA mode of SLG is split into the ZA and ZO′ modes in bilayer graphene or graphite. ZO′ represents a breathing mode between adjacent layers. We find that even such a small splitting can result in a large reduction of the phonon population, as shown in figure 2.19. Due to the splitting, the phase space of the four-ZA process becomes 1/16 of that in SLG, being unimportant. This explains the fact that the three-phonon thermal conductivity prediction of graphite agrees well with experiments [84, 97]. Regarding the second question, we need to refer to the reflection symmetry. The five-phonon process can at most involve four ZA modes, the same as four-phonon scattering. Without increasing the population, the higher order makes the five-phonon scattering negligible compared to four-phonon scattering.

2.5 Further discussion

2.5.1 Scaling with frequency

Due to the simplicity, scaling laws of phonon scattering rates are very useful in thermal nanoengineering. For example, the power laws of three-phonon scattering $\tau_3^{-1} \sim \omega^2 T$ and phonon–defect scattering $\tau_d^{-1} \sim \omega^4$ have been widely used for advanced thermoelectric materials in understanding experimental thermal conductivity [98–100]. Therefore, it is important to have a scaling law $\tau_4^{-1} \sim \omega^\beta T^2$ for four-phonon scattering. In the early literature [18, 101], β was taken as 2 by using drastic

approximations. The fittings of diamond, Si and BAs in figure 2.23 show that the value of β varies from 2 to 4. In comparison, τ_3^{-1} has a more dispersed distribution with a frequency, and the scaling law $\tau_3^{-1} \sim \omega^2 T$ cannot fit all the data well simultaneously, while τ_4^{-1} has a more concentrated distribution and the scaling law can fit all the phonons well. This is because the selection rules in four-phonon processes can be more easily satisfied, that is, they become less restrictive and less dependent on the dispersive nature of the phonon frequency.

2.5.2 Strong Umklapp scattering

The difference between iterative and RTA thermal conductivities comes from subtle differences in the normal and Umklapp processes. Umklapp processes provide thermal resistance, degradation of a flowing distribution of phonons. Normal processes do not degrade the overall current but play the important role of redistributing thermal energy among various modes in the system. If normal processes dominate over Umklapp processes, the RTA solution does not accurately represent κ as it treats normal processes as purely resistive and underestimates κ [9]. As shown in figure 2.24, three-phonon scattering is dominated by normal processes in diamond and BAs, not so in Si. Thus, diamond and BAs require an exact solution for three-phonon scattering [9]. As for four-phonon scattering, all three materials show dominant Umklapp processes over normal processes. Thus, treating the four-phonon scattering at the RTA level for most materials within the iteration scheme is probably a good approximation.

2.5.3 Negligible three-phonon scattering to the second order

We note that two three-phonon processes, $\lambda + \lambda_1 \rightarrow \lambda'$ and $\lambda' \rightarrow \lambda_2 + \lambda_3$, may be combined to give the three-phonon scattering to the second order, which is another type of fourth-order process [34, 101], as shown in figure 2.25 (b). Here, λ' is an intermediate virtual state. The energy is conserved from the initial state $\lambda + \lambda_1$ to the final state $\lambda_2 + \lambda_3$, while the energy is not necessarily conserved in the first step or in the second step alone [34]. The energy denominators of three-phonon scattering

$$\frac{\langle i|\hat{H}_3|f\rangle}{|E_i - E_f|} \tag{2.56}$$

and four-phonon scattering

$$\frac{\langle i|\hat{H}_4|f\rangle}{|E_i - E_f|} \tag{2.57}$$

vanish due to the energy conservation law $E_i = E_f$. In contrast to equations (2.56) and (2.57), the transition matrix element in the combined three-phonon process is

$$\frac{\langle i|\hat{H}_3|\mathrm{vir}\rangle\langle \mathrm{vir}|\hat{H}_3|f\rangle}{|E_i - E_{\mathrm{vir}}|}. \tag{2.58}$$

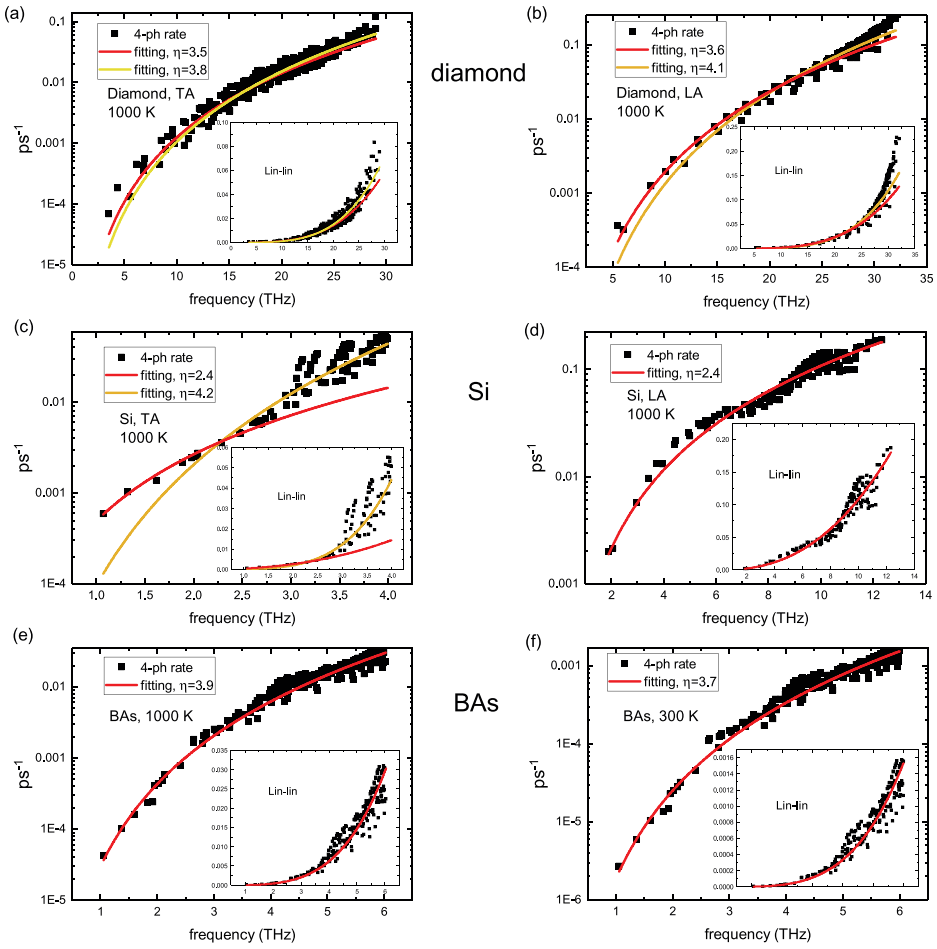

Figure 2.23. Power law fitting $\tau_4^{-1} = A\omega^{\beta}$ of the acoustic phonons in diamond, Si and BAs calculated from first principles. Each panel is plotted in a log–linear scale to give a clear view of the low-frequency behavior, while the inset is in linear–linear scale for a clearer view of the high-frequency behavior. (a) and (b) are the TA and LA modes of diamond at 1000 K, respectively. (c) and (d) are the TA and LA modes of Si at 1000 K, respectively. (e) and (f) are the acoustic modes of BAs at 1000 and 300 K, respectively. We note that four-phonon scattering is only important for diamond and Si at higher temperatures. For each of (a), (b) and (c), we have two fitting curves: the red curve (lower power) fits the low-frequency behavior better, while the yellow curve (higher power) fits better in the higher-frequency range. Reproduced with permission from [27]. Copyright 2017 the American Physical Society.

$|\text{vir}\rangle$ is the intermediate virtual state. The discussion of the denominator in equation (2.58) can be divided into two cases. In case 1, the energy is not conserved in the first or the second step [34]. The energy denominators for the transition are not small. Therefore, the transition rate is not considered to be large, as discussed in [102]. In case 2, the energy conservation condition for the first step is nearly satisfied or satisfied. This process was named 'resonance in three-phonon scattering' and is

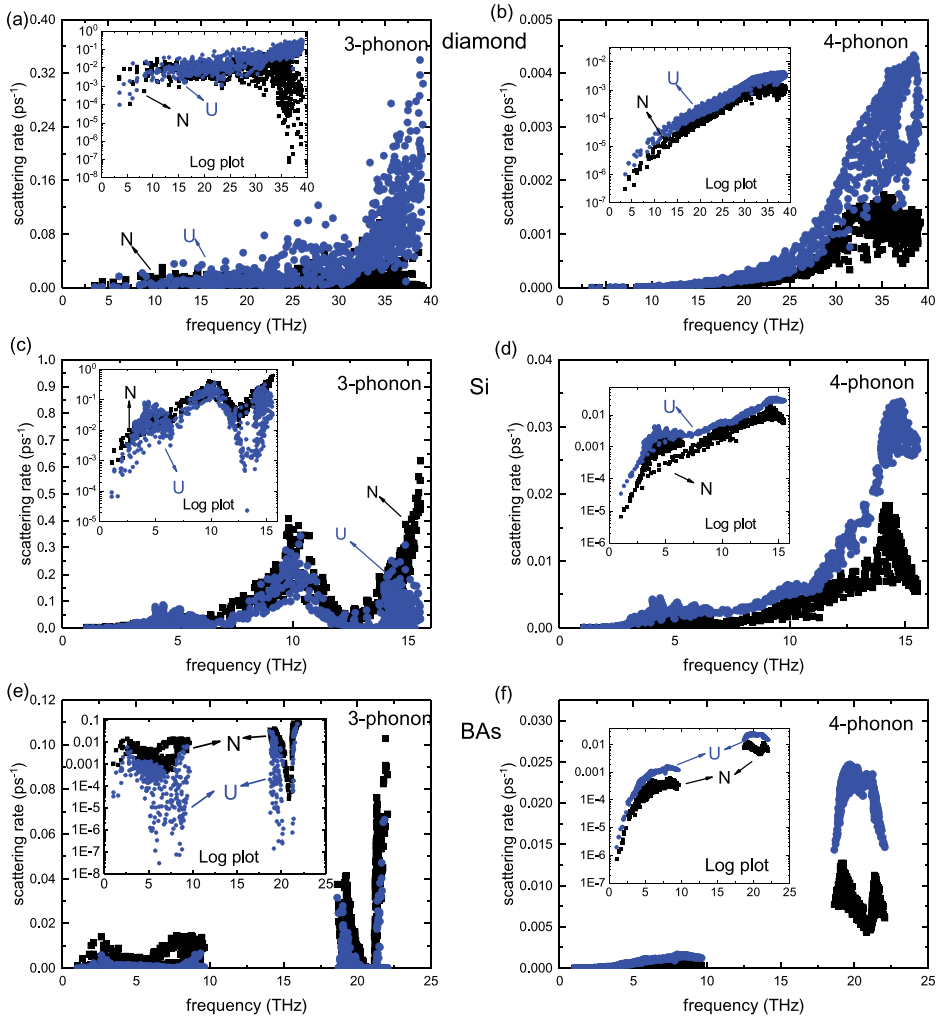

Figure 2.24. Comparison between normal and Umklapp scattering rates for diamond, Si and BAs at $T = 300$ K calculated from first-principles. Each panel is plotted in a linear–linear scale, while each inset is in a log–linear scale. Reproduced with permission from [27]. Copyright 2017 the American Physical Society.

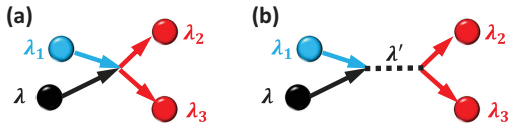

Figure 2.25. The diagram examples for the comparison between (a) the intrinsic four-phonon scattering and (b) the three-phonon scattering to the second order. Reproduced with permission from [26].

discussed by Carruthers [102]. In this case, although the scattering is in the same order as the intrinsic four-phonon scattering, the number of scattering events that satisfy the energy and momentum selection rule is only 10^{-3}–10^{-5} of that in the intrinsic four-phonon scattering in our study. This is because the resonant three-phonon scattering has a strong requirement that the intermediate state has to be an existing phonon mode in the **q**-mesh, while the intrinsic four-phonon scattering has no such requirement. For example, for Si with a $16 \times 16 \times 16$ **q**-mesh and the energy-conservation-tolerant range of 1.24 meV (0.3 THz), the TA mode at $\mathbf{q}^* = (0.5,0,0)$ has 4.6×10^7 intrinsic four-phonon events, and only 2.7×10^4 resonant three-phonon events. For the TA mode at $\mathbf{q}^* = (0.625,0,0)$, the number of intrinsic four-phonon events is similarly about 4.6×10^7, while the number of resonant three-phonon events is only 36. Therefore, the overall three-phonon to the second-order scattering rate is negligible compared to the intrinsic four-phonon scattering. We note that this conclusion is consistent with the conjecture in the literature [101].

2.6 Summary and outlook

In summary, predictive calculation of four-phonon scattering realized since 2016 has enabled the accurate prediction of thermal conductivity for a broader scope of materials over a much wider temperature range. Generally speaking, strong four-phonon scattering is originated from either a large scattering potential (e.g., a large phonon population or strong anharmonicity) or a large scattering phase space, or both. Based on these two origins, table 2.1 summarizes the categories and examples in which four-phonon scattering is strong.

The large scattering potential is induced by either high temperature or intrinsic strongly anharmonic interatomic bonding. The former is seen in general solids. Actually, raising temperature not only increases anharmonicity but also excites a greater phonon population that can boost four-phonon scattering. The latter could be found in many technically important materials, such as most inorganic thermoelectric materials. In addition, the rocksalt compounds generally have long-ranged resonant interaction that causes strong anharmonicity. Among them, PbTe and NaCl have been recently found to have strong four-phonon scattering at room temperature, while the others also need further investigation.

The large four-phonon scattering phase space is either caused by relatively restricted three-phonon scattering phase space or large DOS. The former is seen in the materials with a large acoustic–optical band gap and the two-dimensional materials with reflection symmetry. The latter is seen for high-frequency phonons, in particular optical phonons which are usually bunched together and allow a large $\lambda_1 + \lambda_2 \rightarrow \lambda_3 + \lambda_4$ scattering phase space.

Despite the advances of four-phonon scattering calculation in the past few years, its impact on a broader range of materials is still open to be examined. Some immediate examples are the materials showing ultra-low thermal conductivity, such as the halides (LiF, LiCl, LiBr, LiI, NaF, NaBr, NaI, KF, KCl, KBr, KI, RbF,

Table 2.1. The categories and examples in which four-phonon scattering is significant based on the two fundamental origins.

Origins	Categories	Applications	Examples examined	To be examined
Strong scattering potential (strong anharmonicity)	High temperature	Thermal barrier coating, nuclear materials, high-T thermoelectrics	In general	In general
	Strongly anharmonic (low-κ) materials	Thermoelectrics, thermal barrier coating, thermal energy storage, phase change materials	Ar, PbTe, NaCl	Rocksalt compounds, halides, hydrides, chalcogenides, oxides, others (Bi, Sb), etc
Large scattering phase space	With large acoustic–optical phonon band gap	Thermal management	BAs, AlP, AlAs, AlSb, c-GaN, GaP, GaAs, GaSb, InP, nAs, InSb, etc	I–VII, II–VI binary compounds with large mass ratio
	2D materials with reflection symmetry	Thermal management, surface plasmon	Single-layer graphene	Single-layer h-BN
	Large DOS: e.g. optical phonons	Infrared (sensing, radiative cooling, energy harvesting, metamaterials), hot electron relaxation, complex crystals (perovskites, MXenes, etc)	In general	In general

RbCl, RbBr, RbI, CsF, CsCl, CuCl, CuI, AgI, etc), hydrides (LiH, NaH, KH, RbH, CuH, etc), chalcogenides (CdSe, BaTe, CdTe, BaS, PbS, PbSe, Bi_2Te_3, SnS, SnSe, SnTe, GeTe, etc) and oxides (CdO, SrO, BaO, etc) [12]. Most of them have a rocksalt structure, and few are zinc-blende or wurtzite. The calculation of four-phonon scattering in these materials is straightforward since most crystal structures are simple, with only two basis atoms in a unit cell. Apart from these, it is also interesting to examine complex crystals such as perovskites and MXenes (transition metal carbides, nitrides, or carbonitrides), in which there are many optical branches. The impact of phonon renormalization on three- and four-phonon scattering urgently needs to be explored in more materials as they both are a representation of anharmonicity and coupled together with each other. Another interesting direction is to explore the interplay between four-phonon scattering and other factors such as pressure [103], interfaces and defects. In addition, we also look forward to seeing the exploration of other origins that could lead to strong four-phonon scattering and new thermal transport phenomena.

For ultra-low thermal conductivity materials, an open question is about the nature of thermal transport since four-phonon scattering could bring the phonon mean free path down below the interatomic distance, i.e., the Ioffe–Regel limit. Recently, it was found that for some single crystals such as Tl_3VSe_4, $YbFe_4Sb_{12}$, $CsSnI_3$, $CsPbI_3$ and $CsPbBr_3$, even three-phonon scattering could significantly underestimate the thermal conductivity at room temperature [104]. We suspect that the inclusion of the four-phonon scattering could bring the predicted thermal conductivity even lower. Therefore, the particle nature of phonon thermal transport still needs more investigation and better understanding when four-phonon scattering is included.

With the accurate prediction of phonon–phonon scattering rate enabled by adding four-phonon processes, a variety of processes that involve both phonon–phonon scattering and the scattering between phonons and other particles such as electrons, photons and polaritons could be re-investigated. As already discussed in this chapter, the prediction of infrared properties was significantly improved. We foresee that it will also generate an impact on the understanding and prediction of the laser heating process, hot electron relaxation, interfacial thermal transport, electrical transport, etc.

For many years, researchers have been devoted to the search for materials with extreme thermal properties, e.g., ultra-low or ultra-high thermal conductivity, due to the intriguing physics and promising cutting-edge applications. We anticipate that the generalization of four-phonon scattering calculation will create many opportunities towards this goal. With the rapid increase of the computational power, application of the three- and four-phonon scattering will generate significantly more impact on the prediction of thermal transport as well as other phonon-related applications.

References

[1] Maradudin A A and Flinn P A 1961 Anharmonic contributions to vibrational thermodynamic properties of solids: Part I *Ann. Phys.* **15** 337–59

[2] Maradudin A A and Fein A E 1962 Scattering of neutrons by an anharmonic crystal *Phys. Rev.* **128** 2589

[3] Maradudin A A, Fein A E and Vineyard G H 1962 On the evaluation of phonon widths and shifts *Phys. Status Solidi* B **2** 1479–92

[4] Debernardi A, Baroni S and Molinari E 1995 Anharmonic phonon lifetimes in semiconductors from density-functional perturbation theory *Phys. Rev. Lett.* **75** 1819–22

[5] Bechstedt F, Käckell P, Zywietz A, Karch K, Adolph B, Tenelsen K and Furthmüller J 1997 Polytypism and properties of silicon carbide *Phys. Status Solidi* B **202** 35–62

[6] Debernardi A 1998 Phonon linewidth in III–V semiconductors from density-functional perturbation theory *Phys. Rev.* B **57** 12847–58

[7] Lang G, Karch K, Schmitt M, Pavone P, Mayer A, Wehner R and Strauch D 1999 Anharmonic line shift and linewidth of the Raman mode in covalent semiconductors *Phys. Rev.* B **59** 6182–8

[8] Tang X and Fultz B 2011 First-principles study of phonon linewidths in noble metals *Phys. Rev.* B **84** 054303

[9] Broido D A, Malorny M, Birner G, Mingo N and Stewart D A 2007 Intrinsic lattice thermal conductivity of semiconductors from first principles *Appl. Phys. Lett.* **91** 231922

[10] Esfarjani K, Chen G and Stokes H T 2011 Heat transport in silicon from first-principles calculations *Phys. Rev.* B **84** 085204

[11] Lindsay L, Broido D A and Reinecke T L 2013 First-principles determination of ultrahigh thermal conductivity of boron arsenide: a competitor for diamond? *Phys. Rev. Lett.* **111** 025901

[12] Seko A, Togo A, Hayashi H, Tsuda K, Chaput L and Tanaka I 2015 Prediction of low-thermal-conductivity compounds with first-principles anharmonic lattice-dynamics calculations and Bayesian optimization *Phys. Rev. Lett.* **115** 205901

[13] Feng T and Ruan X 2014 Prediction of spectral phonon mean free path and thermal conductivity with applications to thermoelectrics and thermal management: a review *J. Nanomater.* **2014** 206370

[14] Bao H, Chen J, Gu X and Cao B 2018 A review of simulation methods in micro/nanoscale heat conduction *ES Energy Environ.* **1** 16

[15] Lindsay L, Hua C, Ruan X and Lee S 2018 Survey of *ab initio* phonon thermal transport *Mater. Today Phys.* **7** 106–20

[16] Tong Z, Liu L, Li L and Bao H 2018 Temperature-dependent infrared optical properties of 3c-, 4h- and 6h-SiC *Physica* B **537** 194–201

[17] Joshi Y P, Tiwari M D and Verma G S 1970 Role of four-phonon processes in the lattice thermal conductivity of silicon from 300 to 1300 K *Phys. Rev.* B **1** 642–6

[18] Ecsedy D and Klemens P 1977 Thermal resistivity of dielectric crystals due to four-phonon processes and optical modes *Phys. Rev.* B **15** 5957

[19] Bao H, Qiu B, Zhang Y and Ruan X 2012 A first-principles molecular dynamics approach for predicting optical phonon lifetimes and far-infrared reflectance of polar materials *J. Quant. Spectrosc. Radiat. Transf.* **113** 1683–8

[20] Yang X, Feng T, Kang J S, Hu Y, Li J and Ruan X 2019 Role of higher-order phonon scattering in the zone-center optical phonon linewidth and the Lorenz oscillator model (arXiv 1908.05121)
[21] Novikov M, Ositinskaya T, Shulzhenko O, Podoba O, Sokolov O and Petrusha I 1983 Heat-conductivity of cubic boron–nitride single-crystals *Dopov. Akad. Nauk Ukrain. RSR Seriya* A 72–5
[22] Zhao L-D, Lo S-H, Zhang Y, Sun H, Tan G, Uher C, Wolverton C, Dravid V P and Kanatzidis M G 2014 Ultralow thermal conductivity and high thermoelectric figure of merit in SnSe crystals *Nature* **508** 373–7
[23] Guo R, Wang X, Kuang Y and Huang B 2015 First-principles study of anisotropic thermoelectric transport properties of IV–VI semiconductor compounds SNSE and SNS *Phys. Rev.* B **92** 115202
[24] Lindsay L and Broido D A 2008 Three-phonon phase space and lattice thermal conductivity in semiconductors *J. Phys. Condens. Matter* **20** 165209
[25] Turney J, Landry E, McGaughey A and Amon C 2009 Predicting phonon properties and thermal conductivity from anharmonic lattice dynamics calculations and molecular dynamics simulations *Phys. Rev.* B **79** 064301
[26] Feng T and Ruan X 2016 Quantum mechanical prediction of four-phonon scattering rates and reduced thermal conductivity of solids *Phys. Rev.* B **93** 045202
[27] Feng T, Lindsay L and Ruan X 2017 Four-phonon scattering significantly reduces intrinsic thermal conductivity of solids *Phys. Rev.* B **96** 161201
[28] Kang J S, Li M, Wu H, Nguyen H and Hu Y 2018 Experimental observation of high thermal conductivity in boron arsenide *Science* **361** 575–8
[29] Li S, Zheng Q, Lv Y, Liu X, Wang X, Huang P Y, Cahill D G and Lv B 2018 High thermal conductivity in cubic boron arsenide crystals *Science* **361** 579–81
[30] Tian F *et al* 2018 Unusual high thermal conductivity in boron arsenide bulk crystals *Science* **361** 582–5
[31] Feng T and Ruan X 2018 Four-phonon scattering reduces intrinsic thermal conductivity of graphene and the contributions from flexural phonons *Phys. Rev.* B **97** 045202
[32] Xia Y 2018 Revisiting lattice thermal transport in PBTE: the crucial role of quartic anharmonicity *Appl. Phys. Lett.* **113** 073901
[33] Ravichandran N K and Broido D 2018 Unified first-principles theory of thermal properties of insulators *Phys. Rev.* B **98** 085205
[34] Ziman J M 1960 *Electrons and Phonons* (London: Oxford University Press)
[35] Kaviany M 2008 *Heat Transfer Physics* (New York: Cambridge University Press)
[36] Klemens P 1958 *Solid State Physics* vol 7 (New York: Academic)
[37] Tamura S-I 1983 Isotope scattering of dispersive phonons in Ge *Phys. Rev.* B **27** 858
[38] Casimir H B G 1938 Note on the conduction of heat in crystals *Physica* **5** 495–500
[39] Berman R, Simon F E and Ziman J M 1953 The thermal conductivity of diamond at low temperatures *Proc. R. Soc. Lond.* A **220** 171–83
[40] Berman R, Foster E L and Ziman J M 1955 Thermal conduction in artificial sapphire crystals at low temperatures. I. Nearly perfect crystals *Proc. R. Soc. Lond.* A **231** 130–44
[41] Omini M and Sparavigna A 1995 An iterative approach to the phonon Boltzmann equation in the theory of thermal conductivity *Physica* B **212** 101–12
[42] Omini M and Sparavigna A 1997 Heat transport in dielectric solids with diamond structure *Nuovo Cimento Soc. Ital. Fis.* D **19D** 1537–63

[43] Broido D A, Ward A and Mingo N 2005 Lattice thermal conductivity of silicon from empirical interatomic potentials *Phys. Rev.* B **72** 014308
[44] Togo A and Tanaka I 2015 First principles phonon calculations in materials science *Scr. Mater.* **108** 1–5
[45] Tersoff J 1989 Modeling solid-state chemistry: interatomic potentials for multicomponent systems *Phys. Rev.* B **39** 5566–8
[46] Tersoff J 1990 Erratum: Modeling solid-state chemistry: interatomic potentials for multicomponent systems *Phys. Rev.* B **41** 3248
[47] Li W, Mingo N, Lindsay L, Broido D A, Stewart D A and Katcho N A 2012 Thermal conductivity of diamond nanowires from first principles *Phys. Rev.* B **85** 195436
[48] Li W, Lindsay L, Broido D A, Stewart D A and Mingo N 2012 Thermal conductivity of bulk and nanowire $Mg_2Si_xSn_{1-x}$ alloys from first principles *Phys. Rev.* B **86** 174307
[49] Lindsay L, Broido D and Mingo N 2009 Lattice thermal conductivity of single-walled carbon nanotubes: beyond the relaxation time approximation and phonon–phonon scattering selection rules *Phys. Rev.* B **80** 125407
[50] Lindsay L and Broido D A 2012 Theory of thermal transport in multilayer hexagonal boron nitride and nanotubes *Phys. Rev.* B **85** 035436
[51] Lindsay L, Broido D A and Reinecke T L 2012 Thermal conductivity and large isotope effect in GaN from first principles *Phys. Rev. Letters* **109** 095901
[52] Ruf T, Henn R, Asen-Palmer M, Gmelin E, Cardona M, Pohl H-J, Devyatych G and Sennikov P 2000 Thermal conductivity of isotopically enriched silicon *Solid State Commun.* **115** 243–7
[53] Abeles B, Beers D, Cody G and Dismukes J 1962 Thermal conductivity of Ge–Si alloys at high temperatures *Phys. Rev.* **125** 44
[54] Glassbrenner C J and Slack G A 1964 Thermal conductivity of silicon and germanium from 3 K to the melting point *Phys. Rev.* **134** A1058
[55] Feng T, Yang X and Ruan X 2018 Phonon anharmonic frequency shift induced by four-phonon scattering calculated from first principles *J. Appl. Phys.* **124** 145101
[56] Morelli D T, Jovovic V and Heremans J P 2008 Intrinsically minimal thermal conductivity in cubic I–V–vi_2 semiconductors *Phys. Rev. Lett.* **101** 035901
[57] El-Sharkawy A, El-Azm A A, Kenawy M, Hillal A and Abu-Basha H 1983 Thermophysical properties of polycrystalline PBS, PBSE, and PBTE in the temperature range 300–700 K *Int. J. Thermophys.* **4** 261–9
[58] Håkansson B and Andersson P 1986 Thermal conductivity and heat capacity of solid NaCl and NaI under pressure *J. Phys. Chem. Solids* **47** 355–62
[59] McCarthy K A and Ballard S S 1960 Thermal conductivity of eight halide crystals in the temperature range 220 K to 390 K *J. Appl. Phys.* **31** 1410–12
[60] Yukutake H and Shimada M 1978 Thermal conductivity of NaCl, MgO, coesite and stishovite up to 40 kbar *Phys. Earth Planet. Inter.* **17** 193–200
[61] Wei L, Kuo P K, Thomas R L, Anthony T R and Banholzer W F 1993 Thermal conductivity of isotopically modified single crystal diamond *Phys. Rev. Lett.* **70** 3764–7
[62] Onn D G, Witek A, Qiu Y Z, Anthony T R and Banholzer W F 1992 Some aspects of the thermal conductivity of isotopically enriched diamond single crystals *Phys. Rev. Lett.* **68** 2806–9
[63] Olson J R, Pohl R O, Vandersande J W, Zoltan A, Anthony T R and Banholzer W F 1993 Thermal conductivity of diamond between 170 and 1200 K and the isotope effect *Phys. Rev.* B **47** 14850–6

[64] Berman R, Hudson P R W and Martinez M 1975 Nitrogen in diamond: evidence from thermal conductivity *J. Phys. C: Solid State Phys.* **8** L430
[65] Zheng Q, Li S, Li C, Lv Y, Liu X, Huang P Y, Broido D A, Lv B and Cahill D G 2018 High thermal conductivity in isotopically enriched cubic boron phosphide *Adv. Funct. Mater.* **28** 1805116
[66] Yang X, Feng T, Li J and Ruan X 2019 Stronger role of four-phonon scattering than three-phonon scattering in thermal conductivity of III-V semiconductors at room temperature *Phys. Rev.* B **100** 245203
[67] Jeżowski A, Stachowiak P, Plackowski T, Suski T, Krukowski S, Boćkowski M, Grzegory I, Danilchenko B and Paszkiewicz T 2003 Thermal conductivity of GaN crystals grown by high pressure method *Phys. Status Solidi* B **240** 447–50
[68] Hess S, Taylor R, O'Sullivan E, Ryan J, Cain N, Roberts V and Roberts J 1999 Hot carrier relaxation by extreme electron–LO phonon scattering in GaN *Phys. Status Solidi* B **216** 51–5
[69] Gervais F and Piriou B 1975 Temperature dependence of transverse and longitudinal optic modes in the α and β phases of quartz *Phys. Rev.* B **11** 3944–50
[70] Dean K, Sherman W and Wilkinson G 1982 Temperature and pressure dependence of the Raman active modes of vibration of α-quartz *Spectrochim. Acta* A **38** 1105–8
[71] Ulrich C, Debernardi A, Anastassakis E, Syassen K and Cardona M 1999 Raman linewidths of phonons in Si, Ge, and Sic under pressure *Phys. Status Solidi* B **211** 293–300
[72] Herchen H and Cappelli M A 1993 Temperature dependence of the cubic boron nitride Raman lines *Phys. Rev.* B **47** 14193–9
[73] Hadjiev V G, Iliev M N, Lv B, Ren Z F and Chu C W 2014 Anomalous vibrational properties of cubic boron arsenide *Phys. Rev.* B **89** 024308
[74] Lockwood D, Yu G and Rowell N 2005 Optical phonon frequencies and damping in AlAs, GaP, GaAs, InP, InAs and InSb studied by oblique incidence infrared spectroscopy *Solid State Commun.* **136** 404–9
[75] Turner W J and Reese W E 1962 Infrared lattice bands in AlSb *Phys. Rev.* **127** 126–31
[76] McCluskey M D, Haller E E and Becla P 2001 Carbon acceptors and carbon–hydrogen complexes in AlSb *Phys. Rev.* B **65** 045201
[77] Cuscó R, Domènech-Amador N, Novikov S, Foxon C T and Artús L 2015 Anharmonic phonon decay in cubic GaN *Phys. Rev.* B **92** 075206
[78] Irmer G, Wenzel M and Monecke J 1996 The temperature dependence of the LO(T) and TO(T) phonons in GaAs and InP *Phys. Status Solidi* B **195** 85–95
[79] Stimets R W and Lax B 1970 Reflection studies of coupled magnetoplasma–phonon modes *Phys. Rev.* B **1** 4720–35
[80] Hass M and Henvis B 1962 Infrared lattice reflection spectra of III–V compound semiconductors *J. Phys. Chem. Solids* **23** 1099–104
[81] Lindsay L and Broido D A 2011 Enhanced thermal conductivity and isotope effect in single-layer hexagonal boron nitride *Phys. Rev.* B **84** 155421
[82] Lindsay L, Broido D A and Mingo N 2010 Flexural phonons and thermal transport in graphene *Phys. Rev.* B **82** 115427
[83] Lindsay L, Li W, Carrete J, Mingo N, Broido D A and Reinecke T L 2014 Phonon thermal transport in strained and unstrained graphene from first principles *Phys. Rev.* B **89** 155426
[84] Fugallo G, Cepellotti A, Paulatto L, Lazzeri M, Marzari N and Mauri F 2014 Thermal conductivity of graphene and graphite: collective excitations and mean free paths *Nano Lett.* **14** 6109–14

[85] Faugeras C, Faugeras B, Orlita M, Potemski M, Nair R R and Geim A K 2010 Thermal conductivity of graphene in corbino membrane geometry *ACS Nano* **4** 1889–92
[86] Chen S, Wu Q, Mishra C, Kang J, Zhang H, Cho K, Cai W, Balandin A A and Ruoff R S 2012 Thermal conductivity of isotopically modified graphene *Nature Mater.* **11** 203–7
[87] Xu X *et al* 2014 Length-dependent thermal conductivity in suspended single-layer graphene *Nat. Commun.* **5** 3689
[88] Ghosh S, Calizo I, Teweldebrhan D, Pokatilov E P, Nika D L, Balandin A A, Bao W, Miao F and Lau C N 2008 Extremely high thermal conductivity of graphene: prospects for thermal management applications in nanoelectronic circuits *Appl. Phys. Lett.* **92** 151911
[89] Ghosh S, Bao W, Nika D L, Subrina S, Pokatilov E P, Lau C N and Balandin A A 2010 Dimensional crossover of thermal transport in few-layer graphene *Nat. Mater.* **9** 555–8
[90] Vallabhaneni A K, Singh D, Bao H, Murthy J and Ruan X 2016 Reliability of Raman measurements of thermal conductivity of single-layer graphene due to selective electron–phonon coupling: a first-principles study *Phys. Rev.* B **93** 125432
[91] Gu X, Fan Z, Bao H and Zhao C Y 2019 Revisiting phonon–phonon scattering in single-layer graphene *Phys. Rev.* B **100** 064306
[92] Lindsay L and Broido D A 2010 Optimized Tersoff and Brenner empirical potential parameters for lattice dynamics and phonon thermal transport in carbon nanotubes and graphene *Phys. Rev.* B **81** 205441
[93] Xie H, Chen L, Yu W and Wang B 2013 Temperature dependent thermal conductivity of a free-standing graphene nanoribbon *Appl. Phys. Lett.* **102** 111911
[94] Li Q-Y, Takahashi K, Ago H, Zhang X, Ikuta T, Nishiyama T and Kawahara K 2015 Temperature dependent thermal conductivity of a suspended submicron graphene ribbon *J. Appl. Phys.* **117** 065102
[95] Chen S *et al* 2011 Raman measurements of thermal transport in suspended monolayer graphene of variable sizes in vacuum and gaseous environments *ACS Nano* **5** 321–8
[96] Lee J-U, Yoon D, Kim H, Lee S W and Cheong H 2011 Thermal conductivity of suspended pristine graphene measured by Raman spectroscopy *Phys. Rev.* B **83** 081419
[97] Lindsay L, Broido D A and Mingo N 2011 Flexural phonons and thermal transport in multilayer graphene and graphite *Phys. Rev.* B **83** 235428
[98] Kim S I *et al* 2015 Dense dislocation arrays embedded in grain boundaries for high-performance bulk thermoelectrics *Science* **348** 109–14
[99] Hong M, Chasapis T C, Chen Z-G, Yang L, Kanatzidis M G, Snyder G J and Zou J 2016 *n*-type $Bi_2Te_{3-x}Se_x$ nanoplates with enhanced thermoelectric efficiency driven by wide-frequency phonon scatterings and synergistic carrier scatterings *ACS Nano* **10** 4719
[100] Xu B *et al* 2017 Nanocomposites from solution-synthesized PbTe–BiSbTe nanoheterostructure with unity figure of merit at low–medium temperatures (500–600 K) *Adv. Mater.* **29** 1605140
[101] Joshi Y P, Tiwari M D and Verma G S 1969 Role of four-phonon processes in the lattice thermal conductivity of silicon from 300 to 1300 K *Phys. Rev.* B **1** 642
[102] Carruthers P 1962 Resonance in phonon–phonon scattering *Phys. Rev.* **125** 123–5
[103] Ravichandran N K and Broido D 2019 Non-monotonic pressure dependence of the thermal conductivity of boron arsenide *Nat. Commun.* **10** 827
[104] Mukhopadhyay S, Parker D S, Sales B C, Puretzky A A, McGuire M A and Lindsay L 2018 Two-channel model for ultralow thermal conductivity of crystalline Tl_3VSe_4 *Science* **360** 1455–8